

# Simulation of primordial object formation

Todd M. Fuller and H. M. P. Couchman<sup>1</sup>

`tfuller@astro.uwo.ca`

`couchman@mcmaster.ca`

*Department of Physics and Astronomy, University of Western Ontario  
London, ON N6A 3K7, Canada*

## ABSTRACT

We have included the chemical rate network responsible for the formation of molecular Hydrogen in the  $N$ -body hydrodynamic code, Hydra, in order to study the formation of the first cosmological objects at redshifts between 10 and 50. We have tested our implementation of the chemical and cooling processes by comparing  $N$ -body top hat simulations with theoretical predictions from a semi-analytic model and found them to be in good agreement. We find that post-virialization properties are insensitive to the initial abundance of  $\text{H}_2$ . Our main objective was to determine the minimum mass ( $M_{SG}(z)$ ) of perturbations that could become self gravitating (a prerequisite for star formation), and the redshift at which this occurred. We have developed a robust indicator for detecting the presence of a self-gravitating cloud in our simulations and find that we can do so with a baryonic particle mass-resolution of  $40M_\odot$ . We have performed cosmological simulations of primordial objects and find that the object's mass and redshift at which they become self gravitating agree well with the  $M_{SG}(z)$  results from the top hat simulations. Once a critical  $\text{H}_2$  fractional abundance of  $\sim 5 \times 10^{-4}$  has formed in an object, the cooling time drops below the dynamical time at the centre of the cloud and the gas free falls in the dark matter potential wells, becoming self gravitating a dynamical time later.

*Subject headings:* cosmology: theory — early universe — galaxies: formation — hydrodynamics — molecular processes

## 1. Introduction

In cold dark matter (CDM) cosmologies, the first objects are expected to form between redshifts of 10 and 50 (Peebles 1993). Radiative cooling via the rotational and vibrational transitions of

---

<sup>1</sup>Department of Physics and Astronomy, McMaster University, Hamilton, ON L8S 4M1, Canada

molecular hydrogen provides the mechanism by which the baryons may first condense in small dark matter potential wells of mass  $\sim 10^6 M_\odot$  and virial temperature  $\sim 1000$  K; too cool for hydrogen line cooling to be effective. Of the several different molecules present in the early universe — for example  $H_2$ , HD, and LiH — molecular hydrogen is the most abundant and dominates cooling between 100 K and 1000 K. Understanding the cooling and formation of the first objects and their influence on subsequent cosmic evolution is an important goal of post-recombination cosmography. Of particular interest is the variety of feedback mechanisms which may operate following the epoch of first star formation.

Even a small number of objects at this early time could have a significant effect on the the entire universe. A fraction of just  $\sim 10^{-5}$  of the baryonic mass condensing into massive stars, would produce sufficient energetic photons to re-ionize the universe (Carr et al. 1984; Couchman & Rees 1985; Loeb 1997). Observations of the CMB provide a limit on the earliest time that reionization could occur. Anisotropies in the CMB on angular scales below the horizon size of  $\sim 10^\circ$  are diminished by free electron production during reionization, and if reionization occurred much before  $z \simeq 50$ , the level of anisotropy in the CMB on ten-degree scales would be lower than is observed (Knox 1998; Shaver et al. 1999).

The mass function of the first stars is very uncertain. Kashlinsky & Rees (1983) argued that the main constituents of primordial objects would be low mass stars, with a few very massive objects (VMOs) of masses  $10^3 - 10^5 M_\odot$  forming at later stages. Other authors (Carr et al. 1984; Loeb 1997) have argued that the lack of cooling by metals increases the Jeans mass and consequently star formation is biased towards the production of high mass stars. Some recent numerical studies (Omukai & Nishi 1998; Bromm et al. 1999) find that the first generation stars are quite massive. Supernovae at the death of high mass stars will contaminate the primordial gas with metals, greatly increasing the ability of the gas to cool, as well as injecting large amounts of kinetic and thermal energy into the pregalactic medium.

The  $H_2$  molecule, with a binding energy of only 4.48 eV, is easily dissociated and UV photons produced by the first objects could quickly destroy all  $H_2$ , even accounting for self-shielding (Haiman et al. 1997). It has been suggested that this might delay further structure formation until larger objects form with non-linear mass scales above  $10^8 M_\odot$  and virial temperatures of  $10^4$  K where hydrogen line cooling dominates. An alternative view is that the elevated electron abundance occurring in the photo-ionized regions around massive stars provides ideal conditions for the re-formation of a substantial  $H_2$  fraction as these regions cool and recombine. In the latter case we might anticipate that further cooling and condensation would be promoted.

In order to assess the nature of the first objects and importance of  $H_2$ -mediated cooling, many authors have simulated the formation of primordial clouds. The computational expense of following several chemical rate equations in 3-D hydrodynamic calculations has resulted in the use of one-dimensional models of cloud collapse by a number of authors. Lepp & Shull (1984), for example, used a spherical model for cloud collapse and followed the chemical reactions responsible

for  $\text{H}_2$  formation. A similar, high resolution (but still 1-D) calculation was undertaken by Haiman et al. (1996). Tegmark et al. (1997) used an even more computationally economical, semi-analytic approach which runs so quickly that the collapse mass versus redshift parameter space could be extensively explored.

One-dimensional approaches, however, neglect the complicated filamentary and sheet-like structures ubiquitous to three-dimensional simulations of CDM universes. With improvements in numerical techniques and computer hardware it is now feasible to undertake realistic high resolution 3-D hydrodynamic simulations which incorporate the relevant chemical reactions. The full three-dimensional approach has been taken by Anninos et al. (1997), and is taken here. Despite the recent successes of 3-D numerical approaches, significant challenges still remain. Adequate modelling of feedback from photo-ionizing radiation and supernova blast waves has not yet been addressed fully self-consistently in a numerical simulation although important first steps have been taken (see for example Gnedin & Ostriker 1997 and Haiman et al. 1999). Second, the shallow slope of the CDM spectrum on scales  $\lesssim 10^8 M_\odot$  leads to a wide range of scales collapsing nearly co-evally and very long-range correlations in the peaks of the mass fluctuation field, posing a severe challenge to the limited dynamic range of 3-D simulations. In this paper we present numerical techniques for modelling the collapse and condensation of gas in dark matter haloes at high redshift with a view to reliably identifying the sites of first star formation. In a subsequent paper we will investigate the effect of feedback of these first stars on the pregalactic medium.

A pre-requisite for star formation in dark-matter-dominated cosmologies is that gas becomes self-gravitating (i.e. the baryon density becomes locally greater than the dark matter density) although this is perhaps not a sufficient condition. The earliest time that stars could then form is the time at which there exist objects that have self-gravitating regions; likely in the core. Identifying these regions in numerical simulations is the key objective of this paper. Our goal is to model primordial objects and determine their mass and the time at which they become self-gravitating within cosmological simulations. This aim distinguishes our approach from that of Bromm et al. (1999) in which the focus is to examine the internal properties of the first self-gravitating clouds.

Structure formation is hierarchical in the CDM model: small objects collapse first and coalesce into larger objects. We may indentify three main stages in the merger hierarchy of the two-component fluid as follows (cf. White & Rees 1978). Initially, the potential gradients resulting from the first small dark matter fluctuations will be very much less than pressure gradients which can be generated in the gas, leading only to small adiabatic density perturbations in the baryonic component. As the dark matter haloes become larger through merging and accretion, the potential gradients will increase to a point at which the baryonic material is compressed to the same fractional overdensity as the dark matter. A dark matter halo is conventionally said to have reached the Jeans mass when this occurs. As the mass of the underlying dark matter haloes increases beyond this point the gas becomes subject to the dominant gravitational influence of the virializing dark matter haloes. This will result in the baryonic matter shock-heating to the effective virial temperature of the dark matter halo and attaining a broadly similar density profile. The subsequent behaviour of

gas in a dark matter halo depends upon the efficiency with which it can cool. In hierarchical models the ratio of the cooling time to the dynamical time is of crucial importance (White & Rees 1978; Blumenthal et al. 1984). If  $t_{cool} \ll t_{dyn}$ , the gas cools efficiently and free falls in the dark matter potential well. Conversely, if  $t_{cool} \gg t_{dyn}$ , the gas is unable to condense appreciably before being incorporated into a larger halo as the hierarchy builds, a process which, in a smooth hierarchy, occurs on a characteristic timescale set by  $t_{dyn}$ . In this paper we demonstrate explicitly these three stages as haloes grow in the CDM hierarchy.

Note that the Jeans mass as used in the above sense for a two component fluid differs from its original definition as the perturbative scale separating acoustic oscillation from instability in a self-gravitating gas. A perturbative treatment of the two component fluid is complicated in detail (see, for example, Meiksin et al. 1999), but we may make a useful simple estimate of the mass scale of a virialized (non-linear) dark matter halo below which baryonic matter is not significantly perturbed, by equating the velocity dispersion of the dark matter in the virialized halo with the specific thermal energy of the gas:

$$\frac{1}{2} \langle v^2 \rangle = \frac{3GM}{5R} = \frac{3kT}{2\mu m_H}. \quad (1)$$

At the Jeans mass the gas has been adiabatically compressed to the same overdensity as the dark matter, implying a baryon temperature  $T = T_b(\delta_v + 1)^{2/3}$ , where  $T_b$  is the background baryon temperature and  $\delta_v$  is the overdensity relative to the background at the time of collapse. The Jeans mass is then approximately

$$M_J = \left( \frac{5kT_0(1+z)}{\mu m_H} \right)^{3/2} \frac{\sqrt{\delta_v + 1}}{2GH_0}, \quad (2)$$

where  $T_0(1+z)^2$  is the temperature of the unperturbed gas at redshift  $z$ .

The outline of the paper is as follows. We discuss the network of chemical reactions involved in the production of molecular hydrogen in § 2, along with the details of its implementation in our  $N$ -body gravitational and gasdynamic code, Hydra (Couchman et al. 1995). As an initial test of our implementation we compare, in § 3, the results of spherically symmetric top hat collapses with an analytic model. In § 4 we determine the minimum mass at a given redshift that an object must have to cool efficiently and collapse to high densities where star formation may begin. This was accomplished by performing many different simulations of top hat perturbations with different masses and overdensities. A more realistic, cosmological simulation is described in section § 5. Here we simulate a  $(25\text{kpc})^3$  volume of space and follow the behaviour of the baryonic component in detail through the three stages of cooling and condensation in hierarchical models as described above.

## 2. Molecular hydrogen cooling and chemistry

The  $\text{H}_2$  molecule has long been known to be an important coolant for gravitational collapse of hydrogen clouds that are cooler than  $T \sim 1000$  K. Gould & Salpeter (1963) discussed formation processes and cooling rates for molecular hydrogen in the interstellar medium; Gould (1964) discussed protostellar collapse through molecular hydrogen cooling.  $\text{H}_2$  is also a key ingredient of the globular cluster formation scenario of Peebles & Dicke (1968). The hydrogen molecule is also important for structure formation in the early universe; the first objects to form have virial temperatures of  $\sim 1000$  K, where the  $\text{H}_2$  molecule is the dominant coolant. Through  $\text{H}_2$  cooling, star clusters (Couchman & Rees 1985) or VMOs (Bond et al. 1984) could form and subsequently reionize the intergalactic medium. Molecular hydrogen is also essential to the formation of the first generation stars (Stahler 1986).

In addition to hydrogen, the primordial gas contained Li, D,  $^3\text{He}$ , and  $^4\text{He}$  with abundances of  $10^{-10}$ ,  $10^{-5}$ ,  $10^{-5}$ , and 0.24 respectively, relative to hydrogen. Line cooling is dominated by neutral hydrogen because the excitation rates of Li, D, and  $^3\text{He}$  are much smaller (Abel et al. 1997).

Molecular hydrogen is the most common molecule at the epoch at which the first primordial stars form (Lepp & Shull 1984). In the ISM molecular hydrogen formation occurs on the surface of grains, but, since stars produce the grains, this cannot be an important mechanism for the first objects. There are, however, other chemical reactions that are able to form  $\text{H}_2$ , which are discussed below. At a redshift of 100, the fractional abundance of molecular hydrogen was  $10^{-6}$  (Galli & Palla 1998). Other molecules that were important coolants are HD and LiH which had abundances  $10^{-3}$  and  $10^{-4}$  times lower than that of  $\text{H}_2$ . The HD molecule becomes the dominant coolant at  $20 \text{ K} \leq T \leq 100 \text{ K}$ , and LiH dominates below 20 K. These two molecules will be important in the coldest and densest gas in an object, and to get to that state the gas initially will radiate thermal energy through  $\text{H}_2$  cooling. Molecular hydrogen cooling is efficient enough to produce self gravitating objects, which is a necessary condition for star formation. Since we are interested in following the evolution of primordial objects only to the self gravitating state where  $\rho_b \approx \rho_{dm}$  and not to higher baryonic densities, we need include only  $\text{H}_2$  cooling and can ignore HD and LiH cooling.

### 2.1. Cooling processes

When an  $\text{H}_2$  molecule collides (usually with neutral hydrogen, the most abundant species) and becomes rotationally or vibrationally excited, it may radiatively de-excite which results in gas cooling, or it may collisionally de-excite which results in no net energy loss from the gas.  $\text{H}_2$  vibrations are excited at 6000 K; below 3000 K only the rotational levels of the molecules can be excited (Puy et al. 1993). Radiative de-excitation dominates at the low densities relevant for primordial gas. In this case,  $\text{H}_2$  molecules are mainly in the ground or first ( $J = 1$ ) rotational state. Collisional excitations are quickly followed by radiative decay. At high densities ( $n = 10^3$

to  $10^4 \text{ cm}^{-3}$  for  $10^2 \text{ K} \leq T \leq 10^4 \text{ K}$ ), collisions dominate and Boltzmann populations are reached. These densities are achieved in the late stages of the collapse of primordial objects.

The cooling mechanisms at various temperatures are shown in figure 1. At temperatures between  $10^2 \text{ K}$  and  $10^4 \text{ K}$  the  $\text{H}_2$  molecule is the most effective coolant. Hollenbach & McKee (1979) express the  $\text{H}_2$  cooling function  $\Lambda_{\text{H}_2}$  in the form

$$\Lambda_{\text{H}_2}[n_H, T] = \frac{\Lambda_{LTE}}{1 + n_{cr}/n_H}, \quad (3)$$

where  $\Lambda_{LTE}$  is the LTE cooling function (see Hollenbach & McKee 1979 for the full expression),  $n_{cr}$  is a critical density defined by:

$$\frac{n_{cr}}{n_H} = \frac{\Lambda_{LTE}}{\Lambda_{\text{H}_2}[n_H \rightarrow 0]}, \quad (4)$$

and  $\Lambda_{\text{H}_2}[n_H \rightarrow 0]$  is the low-density limit of the cooling function. The  $\text{H}_2$  cooling function has been computed by Martin et al. (1996) for  $T > 600 \text{ K}$  and Forrey et al. (1997) for  $T < 600 \text{ K}$ . Galli & Palla (1998) provided a fit to these two computations in the low-density limit, which we adopt here:

$$\log \Lambda_{\text{H}_2}[n_H \rightarrow 0] = -103.0 + 97.59 \log T - 48.05(\log T)^2 + 10.80(\log T)^3 - 0.9032(\log T)^4. \quad (5)$$

There is uncertainty in the  $\text{H}_2$  cooling function because of the difficulty in calculating the interaction potential at low temperatures. Different choices for rotational and vibrational H- $\text{H}_2$  rate coefficients will produce differences in  $\Lambda_{\text{H}_2}$ ; figure 2 illustrates  $\text{H}_2$  cooling rates computed by several authors.

At temperatures between  $10^4 \text{ K}$  and  $5 \times 10^4 \text{ K}$  radiational de-excitation of H dominates the cooling function. We use the expression given by Dalgarno & McCray (1972):

$$\Lambda_{Hline} \sim 7.5 \times 10^{-19} e^{-118348 \text{ K}/T} n^2 f_e (1 - f_e). \quad (6)$$

Cooling processes such as He line cooling and Bremsstrahlung (fig. 1) that operate at higher temperatures may be ignored, since the primordial objects have virial temperatures of  $\sim 1000 \text{ K}$ .

## 2.2. Molecular hydrogen formation and destruction

Despite a relatively small number of elements in the primordial gas, there is a complicated network of reactions involving these elements; Galli & Palla (1998) list 87 reactions in their comprehensive study of the chemistry of the early universe. Fortunately many of these do not affect significantly the collapse of primordial objects and the number of important reactions is much smaller. The HD and LiH molecules are not important at densities in our regime of interest. Helium chemistry and cooling becomes important above  $10^5 \text{ K}$ , which is well above the  $1000 \text{ K}$  virial

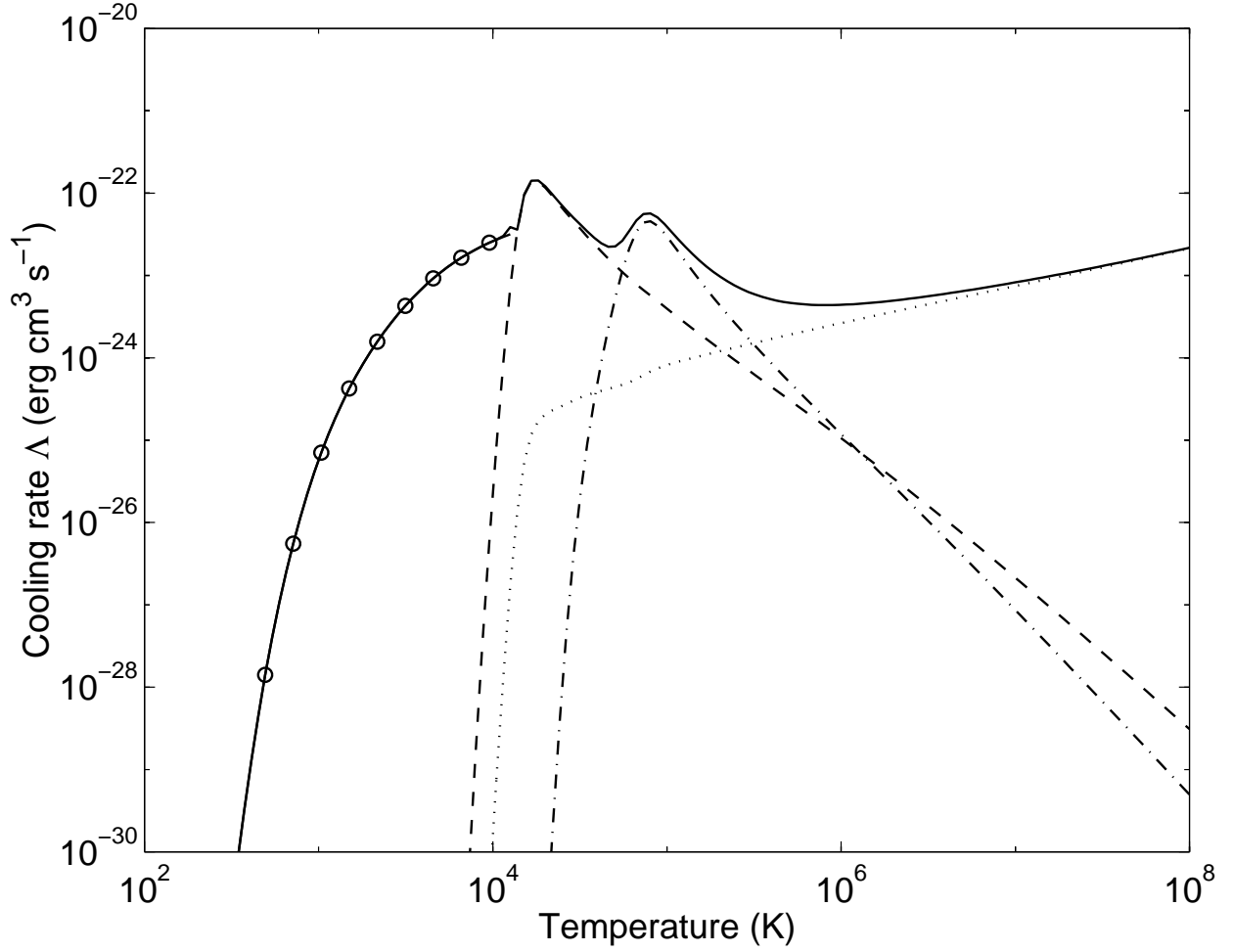


Fig. 1.— Cooling rates for Bremsstrahlung (dotted line), H (dashed line) and He (dash-dotted line) line cooling, and  $\text{H}_2$  (circles) cooling. The  $e^-$ ,  $\text{H}^+$ ,  $\text{He}^+$ , and  $\text{He}^{++}$  abundances were computed assuming collisional equilibrium, and the  $\text{H}_2$  fractional abundance was  $3 \times 10^{-4}$ , which is typical for early objects.

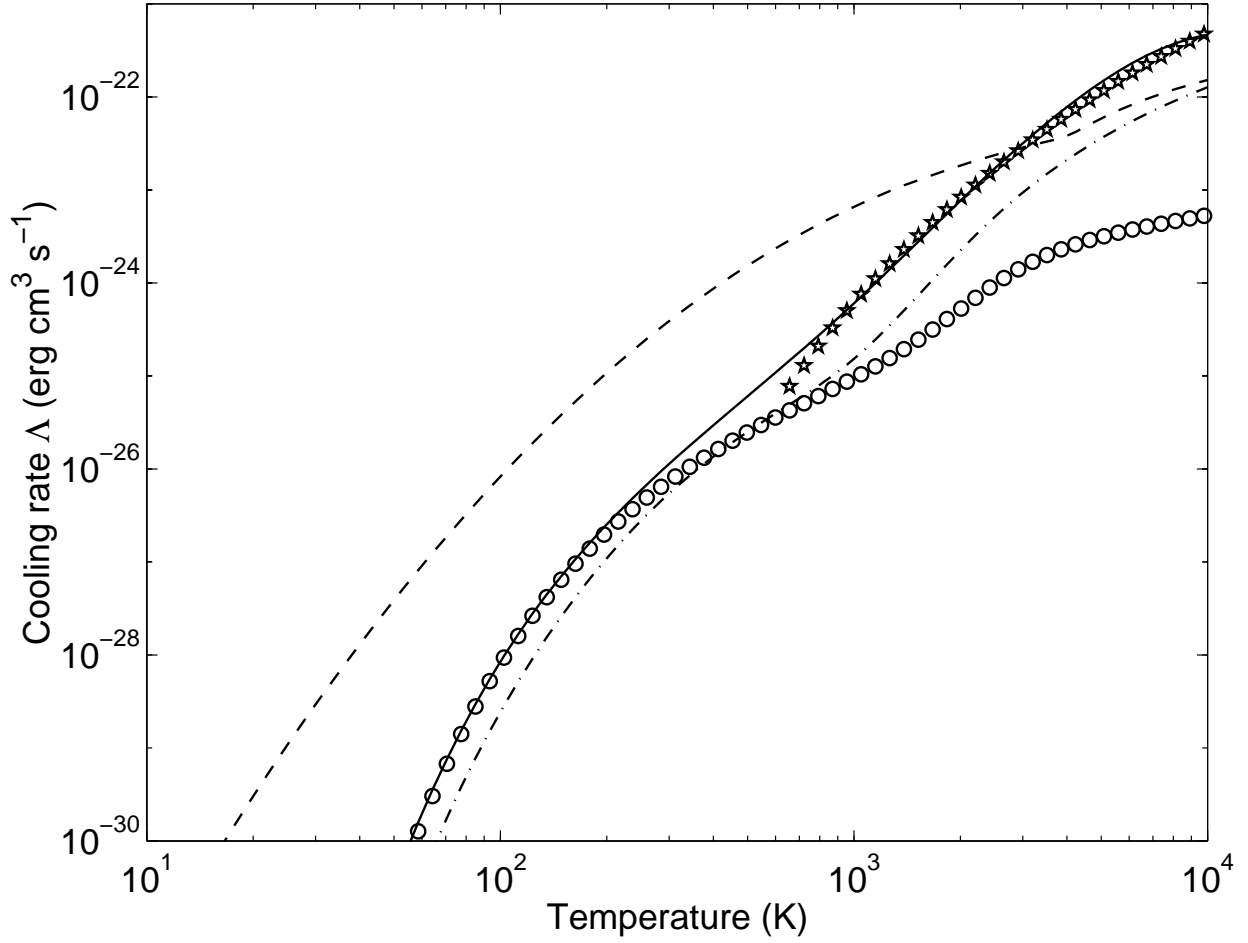


Fig. 2.—  $\text{H}_2$  cooling rates per  $\text{H}_2$  molecule in the low density ( $n < 0.1 \text{ cm}^{-3}$ ) limit, from: Galli & Palla 1998 (solid line), Martin et al. 1996 (stars), Tegmark et al. 1997 (circles), Hollenbach & McKee 1979 (dash-dotted line), and Lepp & Shull 1984 (dashed line).



Table 1. Reactions involved in the formation and destruction of molecular hydrogen.

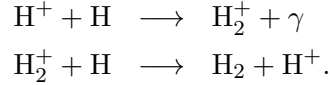
Reaction	Rate	Reference
(1) $\text{H}^+ + \text{e}^- \longrightarrow \text{H} + \gamma$	$1.88 \times 10^{-10} T^{-0.64}$	2, 1(11)
(2) $\text{H} + \text{e}^- \longrightarrow \text{H}^+ + 2\text{e}^-$	see reference	1(11)
(3) $\text{H} + \text{e}^- \longrightarrow \text{H}^- + \gamma$	$1.83 \times 10^{-18} T^{0.88}$	2, 1(12)
(4) $\text{H}^- + \text{H} \longrightarrow \text{H}_2 + \text{e}^-$	$1.3 \times 10^{-9}$	3, 1(10)
(5) $\text{H}^- + \text{e}^- \longrightarrow \text{H} + 2\text{e}^-$	$1.6 \times 10^{-6} (1 + 34/T^{5/6}) \exp(-65/T^{1/3})$	3, 1(10)
(6) $\text{H}_2 + \text{e}^- \longrightarrow 2\text{H} + \text{e}^-$	$5.6 \times 10^{-11} T^{1/2} \exp(-102124/T)$	1(13)
(7) $\text{H}_2 + \text{H}^+ \longrightarrow \text{H}_2^+ + \text{H}$	$2.6 \times 10^{-8} \exp(-2.12/T_4)/T^{1/2}$	8, 1
(8) $\text{H}^- + \text{H}^+ \longrightarrow 2\text{H}$	$4 \times 10^{-6}/T^{1/2}$	7, 1(15)
(9) $\text{H} + \text{H} \longrightarrow \text{H}_2$	$4 \times 10^{-27}$ @ $T = 100 \text{ K}$	3
(10) $\text{H}_2^+ + \text{H} \longrightarrow \text{H}_2 + \text{H}^+$	$6.4 \times 10^{-10}$	1(5)
(11) $\text{H}_2^+ + \text{H}^- \longrightarrow \text{H}_2 + \text{H}$	$\leq 2.3 \times 10^{-7}$	3, 1(15)
(12) $\text{H}_3^+ + \text{e}^- \longrightarrow \text{H}_2 + \text{H}$	$5 \times 10^{-9}$	6
(13) $\text{H}_2 + \text{H}_2 \longrightarrow \text{H}_2 + 2\text{H}$	$3 \times 10^{-4} \exp(-5.2/T_4)/T^{3/2}$	3
(14) $\text{H}_2 + \text{H}^- \longrightarrow \text{H}_2 + \text{H} + \text{e}^-$	very small	3
(15) $\text{H}_2 + \text{H}_2^+ \longrightarrow \text{H}_3^+ + \text{H}$	$2.1 \times 10^{-9}$	3
(16) $\text{H}_2 + \text{e}^- \longrightarrow \text{H} + \text{H}^-$	$2.7 \times 10^{-8} \exp(-4.3/T_4)/T^{3/2}$	3
(17) $\text{H}_2 + \text{H} \longrightarrow 3\text{H}$	see reference	1(14)
(18) $\text{H}_2^+ + \text{e}^- \longrightarrow 2\text{H}$	$4.2 \times 10^{-8}/T^{1/2}$	6, 1(16)
(19) $\text{H}^+ + \text{H} \longrightarrow \text{H}_2^+ + \gamma$	$1.85 \times 10^{-23} T^{1.8}$	1(4)
(20) $\text{H}^- + \text{H}^+ \longrightarrow \text{H}_2^+ + \text{e}^-$	$2.291 \times 10^{-0.4}$ for $T \leq 2 \times 10^4 \text{ K}$	1(4)
(21) $\text{H}^- + \text{H} \longrightarrow 2\text{H} + \text{e}^-$	see reference	1(10)
(22) $\text{H} + \gamma \longrightarrow \text{H}^+ + \text{e}^-$	see reference	1(17)
(23) $\text{H}^- + \gamma \longrightarrow \text{H} + \text{e}^-$	$0.114 T_\gamma^{2.13} \exp(-8650/T_\gamma)$	9, 1(4)
(24) $\text{H}_2^+ + \gamma \longrightarrow \text{H} + \text{H}^+$	$6.36 \times 10^5 \exp(-71600/T_\gamma)$	9, 1(18)
(25) $\text{H}_2^+ + \gamma \longrightarrow 2\text{H}^+ + \text{e}^-$	see reference	1(4)
(26) $\text{H}_2 + \gamma \longrightarrow \text{H}_2^+ + \text{e}^-$	see reference	1
(27) $\text{H}_2 + \gamma \longrightarrow \text{H}^+ + \text{H} + \text{e}^-$	see reference	19
(28) $\text{H}_2 + \gamma \longrightarrow \text{H}(1s) + \text{H}(2s, 2p)$	see reference	1
(29) $\text{H}_2 + \gamma \longrightarrow 2\text{H}(1s)$	see reference	1

References. — 1: Abel et al. 1997, 2: Hutchins 1976, 3: Hirasawa 1969, 4: Shapiro & Kang 1987, 5: Karpas et al. 1979, 6: Solomon & Werner 1971, 7: Hill & Silk 1975, 8: Rapp & Francis 1962, 9: Tegmark et al. 1997, 10: Janev et al. 1987, 11: Ferland et al. 1992, 12: Wishart 1979, 13: Donahue & Shull 1991, 14: Dove & Mandy 1986, 15: Dalgarno & Lepp 1987, 16: Schneider et al. 1994, 17: Osterbrock 1974, 18: Stancil 1994, 19: Couchman 1986

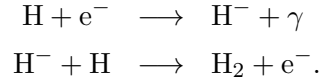
Note. — References in parenthesis are the source used by Abel et al. (1997). Where more than two references are given, the reaction rate listed was obtained from the first.

temperatures that primordial objects have. Ignoring HD, LiH, and He molecular species reduces the number of relevant reactions considerably, and will only limit investigations of the latest stages of baryonic condensation at low temperatures which are not the focus of this paper. We summarize and justify in this section the reactions which it is necessary to include in our numerical model to accurately follow the chemistry and cooling of the first objects.

Molecular hydrogen production proceeds via only two major mechanisms. In the  $\text{H}_2^+$  channel the proton acts as a catalyst:



In the  $\text{H}^-$  channel the electron acts as a catalyst:



For redshifts higher than 200, CMB photons are energetic enough that the reaction  $\text{H}^- + \gamma \longrightarrow \text{H} + \text{e}^-$  neutralizes all  $\text{H}^-$  ions and therefore the  $\text{H}^+$  channel dominates for  $z \gtrsim 200$ . At lower redshifts, the  $\text{H}^-$  channel proceeds much more quickly than the  $\text{H}^+$  channel and dominates  $\text{H}_2$  production.

The destruction of the intermediaries  $\text{H}^-$  and  $\text{H}_2^+$  proceeds much more quickly than their production. This leads to equilibrium fractional abundances of  $\text{H}^-$  and  $\text{H}_2^+$  (relative to total hydrogen number density) of:

$$f_{\text{H}^-} = \frac{k_3 f_{\text{H}} f_{\text{e}^-} + k_{16} f_{\text{H}_2} f_{\text{e}^-}}{k_4 f_{\text{H}} + k_8 f_{\text{H}^+} + k_5 f_{\text{e}^-} + k_{11} f_{\text{H}_2^+} + k_{20} f_{\text{H}^+} + k_{21} f_{\text{H}}} \quad (7)$$

$$f_{\text{H}_2^+} = \frac{k_7 f_{\text{H}_2} f_{\text{H}^+} + k_{19} f_{\text{H}^+} + k_{20} f_{\text{H}^-} f_{\text{H}^+}}{k_{10} + k_{11} f_{\text{H}^-} + k_{18} f_{\text{e}^-}}, \quad (8)$$

where the rate for reaction  $i$  is  $k_i$ . Table 1 lists the reactions we have considered here; where more than one source is listed for the reaction rate, we have used the rate given by Abel et al. (1998).

Reaction rates depend on temperature and the abundances of the reactants, all of which change with time, and therefore these must be known to identify the dominant reactions. This leads to a circular argument: the density and temperature must be known to identify dominant reactions, but the dominant reactions must be known to properly model the density and temperature evolution. One could include every chemical reaction, but this is computationally expensive. Instead, we used reasonable estimates for the chemical abundances, density, and temperature to tentatively identify the important reactions, and included these in our  $N$ -body code, along with the dominant cooling mechanisms; the implementation is discussed in §2.5 below. Then we performed a spherically symmetric top hat collapse of  $10^6 M_{\odot}$  test object (see §3 for details) following the temperature and abundances during the evolution to plot the reaction rates versus redshift in figures 3-5. From these

figures the unimportant reactions may be identified, and their exclusion justified. We believe that our identifications are robust.

Figure 3 shows the  $\text{H}_2$  production and destruction mechanisms along with the temperature of the collapsing object as a function of redshift. The peak temperature occurs at  $1 + z = 20$  when the test object virializes. Although this redshift was arbitrarily chosen, the behaviour of the reactions does not change significantly for perturbations that virialize between  $50 \gtrsim z \gtrsim 10$ , the redshifts at which the first objects are expected to form in models with CDM-like spectra. It is immediately obvious from figure 3 that the only  $\text{H}_2$  production mechanism of importance at these redshifts is the  $\text{H}^-$  channel. The  $\text{H}_3^+$  abundance is less than  $10^{-16}$  (Galli & Palla 1998) so reaction 12 is unimportant. Since the  $\text{H}_2^+$  abundance does not influence the  $\text{H}_2$  production significantly, reactions 10, 11, and 18 may be ignored.

Figure 4 shows the reactions involving the  $\text{H}^-$  ion. Reactions 3 and 4 (the  $\text{H}^-$  channel) are in equilibrium and no other reactions proceed at comparable rates. At  $T > 10^4$  K the  $\text{H}^-$  ion is quickly destroyed by collisions with electrons (reaction 5), thus terminating  $\text{H}_2$  production through this route.

At the low temperatures ( $T \lesssim 5000$  K) encountered in the the first bound objects, there is no efficient means of destroying  $\text{H}_2$ . Although unimportant for objects with virial temperatures of  $T \lesssim 1000$  K,  $\text{H}_2$  dissociation mechanisms must be included for the reaction network to be accurate at higher temperatures. The five  $\text{H}_2$  destruction mechanisms in figure 3 all have similar rates; however at  $T = 5000$  K protons begin to dissociate  $\text{H}_2$  via reaction 7. Once the free electron abundance becomes significant at  $T > 2 \times 10^4$  K,  $\text{H}_2$  dissociation by electrons dominates, with the production of two neutral hydrogen atoms and an electron (reaction 6) strongly favoured over the production of a neutral hydrogen and a negative hydrogen ion (reaction 16). The dissociation of  $\text{H}_2$  by H (reaction 17) is unimportant since almost all hydrogen is ionized at  $T > 2 \times 10^4$  K, at which point  $\text{H}_2$  is dissociated entirely by collisions with free electrons (reaction 6). At lower temperatures dissociation of  $\text{H}_2$  by H is unimportant since charge exchange with  $\text{H}^+$  (reaction 7) occurs at a greater rate.  $\text{H}_2$ - $\text{H}_2$  and  $\text{H}_2$ - $\text{H}_2^+$  collisions are rare because of their low abundance so reactions 13 and 15 are negligible.

Since  $\text{H}_2$  production depends on the free electron abundance, reactions involving the ionization of hydrogen must also be examined. The neutralization of  $\text{H}^+$  by an electron (reaction 1) is in equilibrium with ionization of H by an electron (reaction 2) in figure 5, and these two reactions control the degree of hydrogen ionization.

The dominant reactions thus 1 through 7. All reactions involving helium have been disregarded, which is permissible so long as the temperature is restricted to  $T \lesssim 3 \times 10^4$  K where helium begins ionization and becomes an important coolant. All molecules other than  $\text{H}_2$  (such as LiH and HD and those involving He) have not been included since their abundances are negligible.

The equations that describe the evolution of the various species can be determined using the dominant reactions discussed above. The total particle abundance is  $n = n[\text{H}] + n[\text{H}^+] + 2n[\text{H}_2]$

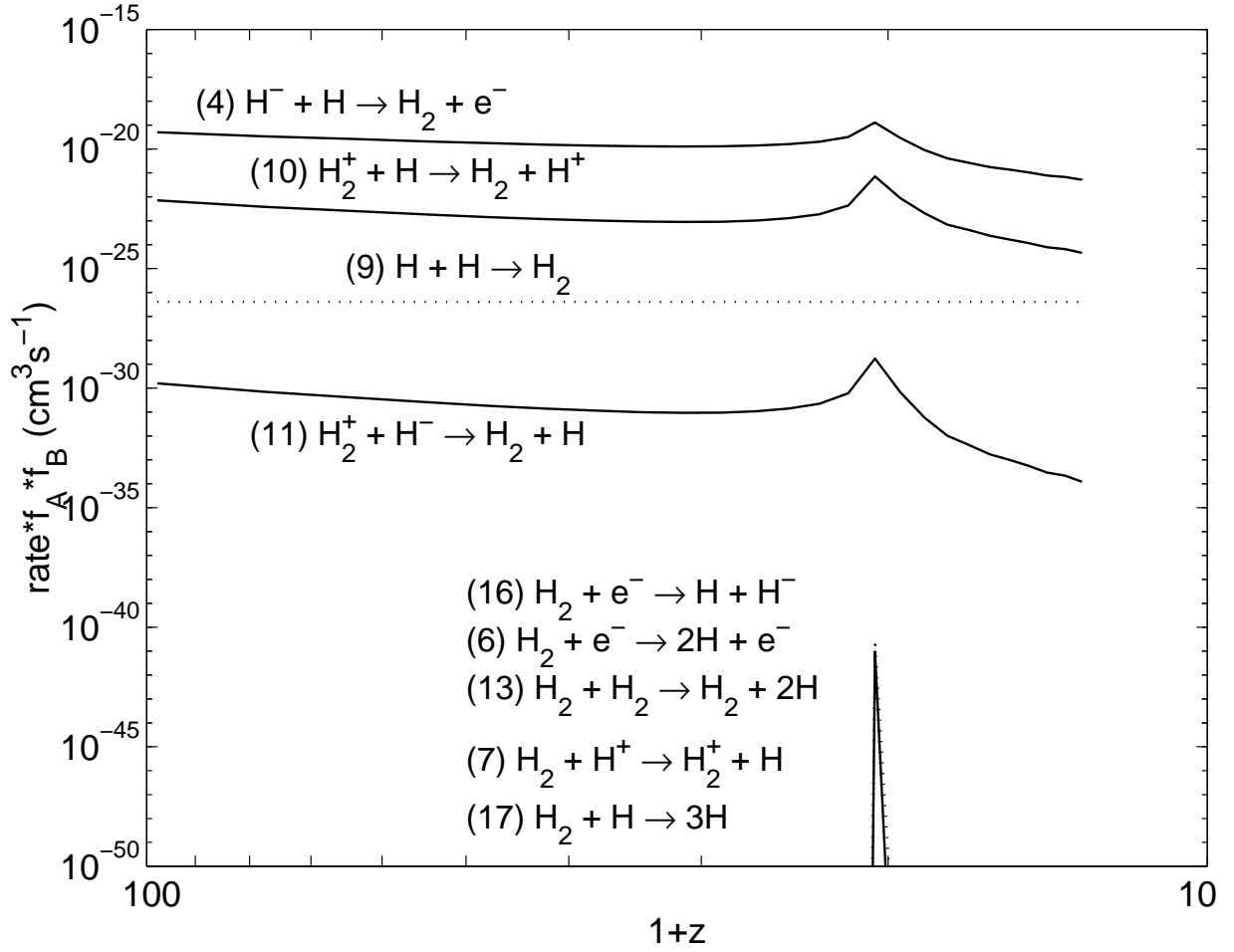


Fig. 3.— Reaction rates for the formation and destruction of molecular hydrogen. Temperatures and fractional abundances of reactants ( $f_A$  and  $f_B$ ) used to compute the rates were taken from a top hat simulation of an early object collapsing at  $1+z = 20$ .  $\text{H}_2$  creation via the  $\text{H}^-$  channel clearly dominates. The five  $\text{H}_2$  destruction reactions all progress at similar rates at these temperatures. The numbers in parentheses indicate the reaction in table 1.

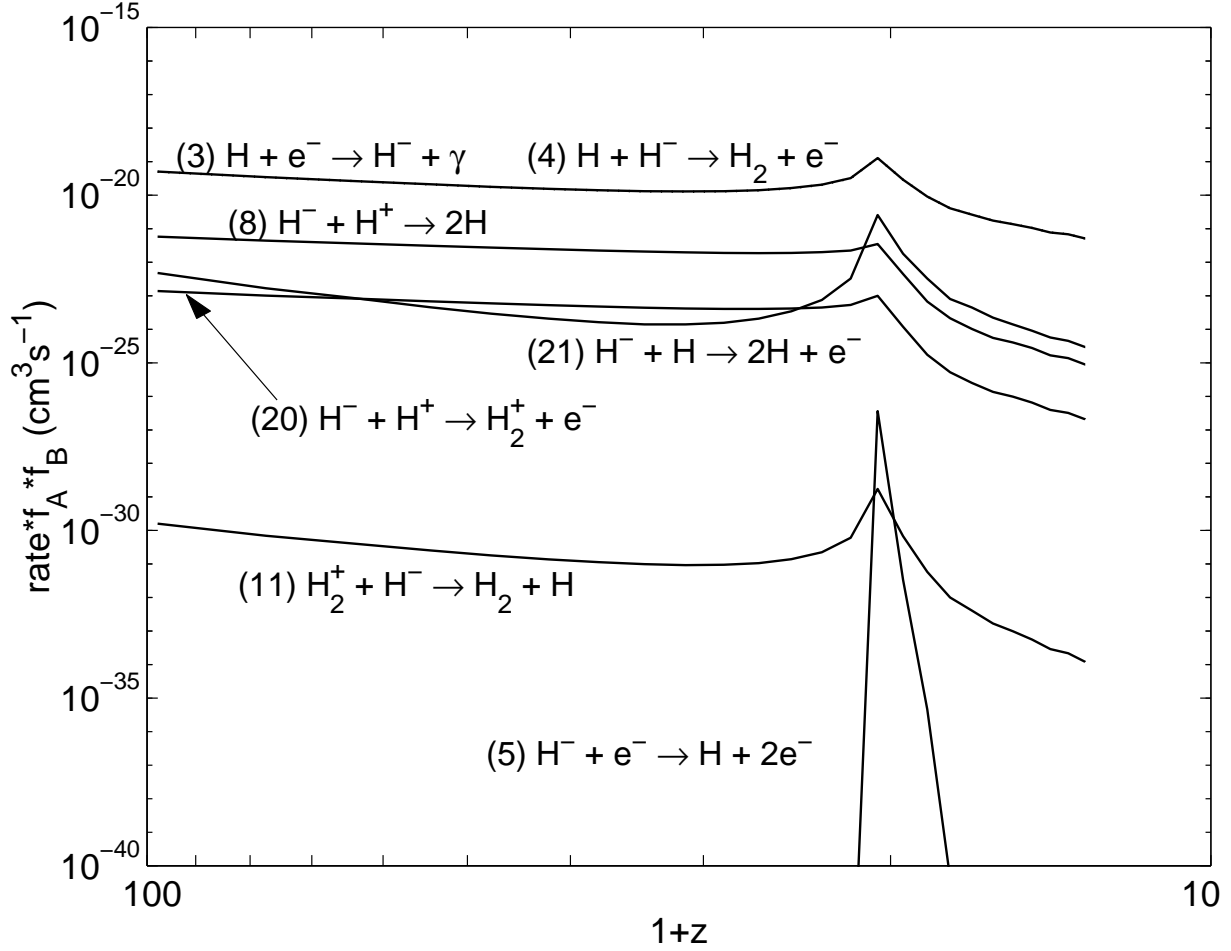


Fig. 4.— Reaction rates for the formation and destruction of  $\text{H}^-$ . The two reactions in the  $\text{H}^-$  channel for molecular hydrogen production (top line) are in equilibrium. At  $T > 10^4 \text{ K}$  the neutralization of  $\text{H}^-$  by  $\text{e}^-$  becomes important. These three reactions exclusively control the  $\text{H}^-$  abundance. The numbers in parentheses indicate the reaction in table 1.

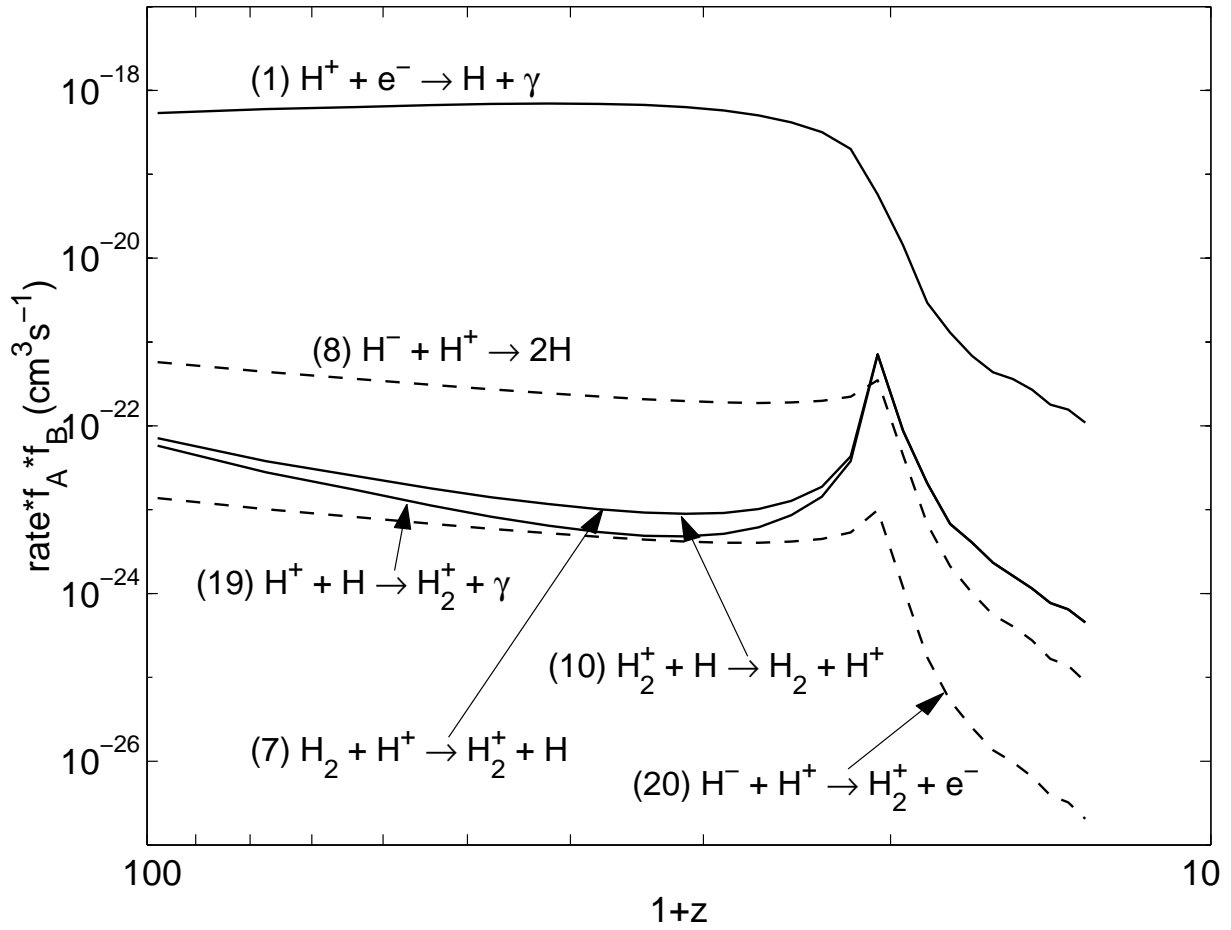


Fig. 5.— Reaction rates involving ionized hydrogen. Radiative recombination controls the  $\text{H}^+$  abundance. The numbers in parentheses indicate the reaction in table 1.

and the fractional abundance of species A is  $f_A = n[A]/n$ . The H, H<sup>+</sup>, and H<sub>2</sub> fractional abundances evolve as:

$$\frac{1}{n} \frac{df_{\text{H}}}{dt} = k_1 f_{\text{H}^+} f_{\text{e}^-} - k_2 f_{\text{H}} f_{\text{e}^-} \quad (9)$$

$$\frac{1}{n} \frac{df_{\text{H}^+}}{dt} = k_2 f_{\text{H}} f_{\text{e}^-} - k_1 f_{\text{H}^+} f_{\text{e}^-} \quad (10)$$

$$\frac{1}{n} \frac{df_{\text{H}_2}}{dt} = k_4 f_{\text{H}^-} f_{\text{H}} - k_7 f_{\text{H}_2} f_{\text{H}^+} - k_6 f_{\text{H}_2} f_{\text{e}^-} \quad (11)$$

Since the H<sup>−</sup> formation and destruction reactions are in equilibrium it is never necessary to integrate the chemical equations to determine its abundance. Note that the H<sup>−</sup> equilibrium abundance (equation 7) may be simplified by including only the rate coefficients for the dominant reactions (i.e.  $k_3, k_4, k_5$ ).

### 2.3. Photoionization and Photodissociation

Although ionization and dissociation by photons are important in the early universe, by  $z = 100$  there are essentially no CMB photons with energies above the thresholds for reactions 22 (13.6 eV) and 23 (0.755 eV). Since H<sub>2</sub><sup>+</sup> becomes important in molecular hydrogen production only at redshifts  $z > 200$ , reactions 24 and 25 may be neglected. The dissociation reactions 26, 27, 28, and 29 are inhibited because the CMB photons are much less energetic than the H<sub>2</sub> binding energy of 4.48 eV. Since there are no sources of energetic photons, all photoionization and photodissociation reactions may be ignored from  $z = 100$  until after the first objects have been formed.

### 2.4. Shocks

There are several issues concerning H<sub>2</sub> chemistry that must be addressed when the gas shocks during collapse. The H<sub>2</sub> molecule has a small binding energy of 4.48 eV, and if a shock has a velocity of  $v \gtrsim \sqrt{2 \times 4.48 \text{ eV} / (2m_p)} \simeq 20 \text{ km/s}$  then H<sub>2</sub> may be collisionally dissociated (Kwan 1977). The first objects to form will have masses between approximately  $10^5 M_\odot$  and  $10^6 M_\odot$  and virial temperatures of  $T \approx 1000 \text{ K}$ . This temperature corresponds to an average thermal velocity  $v = \sqrt{(3kT/2)/(m/2)}$  which is 5 km/s for H and 3.5 km/s for H<sub>2</sub>, well below the collisional dissociation velocity. We have not observed any cases in which the shock velocity approaches the dissociation velocity in our simulations of primordial objects.

### 2.5. Incorporation of the chemical reactions into Hydra

Our  $N$ -body gravitational and gasdynamic code, Hydra, is an adaptive mesh implementation of the smoothed particle hydrodynamics (SPH) algorithm and the particle-particle particle-mesh

(P<sup>3</sup>M) algorithm. A complete description of the code is given by Couchman et al. (1995). The chemical state of the gas is carried by assigning each SPH particle a fractional abundance of H<sub>2</sub> and H<sup>+</sup> as described below.

If the macroscopic changes caused by gravitational and adiabatic heating or cooling operate much more slowly than the chemical processes, then the two become decoupled and may be integrated separately. This is indeed the case for our simulations. During a spherical top hat collapse, the maximum values of  $T/\dot{T}$  and  $\rho/\dot{\rho}$  are on the order of 10<sup>7</sup> and 10<sup>8</sup> years, while  $f_{\text{H}^+}/\dot{f}_{\text{H}^+}$  is approximately 10<sup>4</sup> years.

The time rate-of-change of density is computed for each particle via  $\dot{\rho} = (\rho_i - \rho_{i-1})/dt$  where  $\rho_i$  and  $\rho_{i-1}$  are the density values at the current and previous time step. The value of  $\dot{\rho}$  is assumed to be constant over the time step; while this is not strictly true, the approximation is justified since the time steps are typically a factor of 100 smaller than the characteristic time scale  $\rho/\dot{\rho}$ . The time rate-of-change of temperature from adiabatic processes is computed analogously:  $\dot{T}_{ad,i} = (T_{ad,i} - T_{ad,i-1})/dt$ . These two slowly varying dynamical quantities,  $\dot{\rho}$  and  $\dot{T}_{ad}$ , are needed to compute the rapidly-varying chemical evolution of the system. The cooling functions (fig. 1), adiabatic processes and the chemical abundance equations (9, 10 and 11) are then simultaneously integrated for each particle at every time step. We assume that the H<sup>+</sup> and e<sup>-</sup> abundances are equal, which is justified provided temperatures are constrained to  $T < 10^5$  K. The H<sup>-</sup> abundance may be computed using equation (7). The H<sub>2</sub><sup>+</sup> abundance is never needed since it is not a reactant in any of the dominant reactions. The neutral hydrogen abundance is computed via the conservation equation  $n = n[\text{H}] + n[\text{H}^+] + 2n[\text{H}_2]$ . Of the six species present in the dominant reaction network (e<sup>-</sup>, H, H<sup>-</sup>, H<sup>+</sup>, H<sub>2</sub>, H<sub>2</sub><sup>+</sup>), only two are independent, and each particle therefore carries values for the H<sub>2</sub> and H<sup>+</sup> abundances.

We use the stiff ODE integrator STIFBS from Numerical Recipes (Press et al. 1992). This routine was also chosen for a very similar problem by Haiman et al. (1996) who experimented with other Numerical Recipes routines and found STIFBS to be the most efficient. They also tested the LSODAR routine of Hindmarsh (1983) and found STIFBS  $\approx 20\%$  faster while producing identical results. We compared our integration of the chemical network of ODEs to a stiff ODE integrator in the Matlab software package and found them to agree to 1 part in 10<sup>4</sup>, which is more than adequate for our purposes.



### 3. Tests of the code

#### 3.1. Comparison with analytic models

In this section we present two tests: i) top hat evolution from quiet initial conditions which proceeds to a singular collapse; and ii) a top hat collapse in which perturbations within the top hat overdensity lead to virialization at roughly half the maximum (turnaround) radius.

The top hat model has two free parameters, the initial mass  $M_{TH}$  and the initial overdensity which determines the redshift at which the analytic top hat collapses to a singularity. Using an ODE integrator in the Matlab software package, we numerically integrated the top hat density evolution along with relevant chemical reactions and cooling functions to analytically determine the chemical and temperature evolution of spherical perturbations.

For a simple initial test of the chemical network in Hydra we simulate a spherically symmetric perturbation of uniform density and compare that to the analytic top hat evolution. Particles are placed into the simulation box on a regular lattice, and a spherical region enclosing  $M_{TH}$  is cut out and compressed by an amount that causes the singularity to be reached at the desired redshift. Although placing particles on a regular lattice is unphysical (because it leads to a singularity), the absence of noise in the particle distribution allows an exact comparison between the code and the analytic solution. The particles within the top hat are assigned velocities according to the time derivative of the cycloid equations. The gas particles are given an increase in temperature corresponding to the adiabatic compression.

Figure 6 shows the dark matter, baryon, temperature,  $H^-$ , and  $H_2$  evolution computed using the analytic top hat model and our  $N$ -body code for a top hat perturbation of total mass  $10^6 M_\odot$ . The simulation was terminated prior to  $z = 20$  since there is no point in following the evolution through the singularity. This is however more than sufficient to test the accuracy of the chemistry in the  $N$ -body code. We performed many other simulations using various masses and virialization redshifts, and there was always excellent agreement with the semi-analytic model up to the singularity.

In physical reality the singularity is avoided since random perturbations in the density field will cause non-radial motions to develop, and instead of collapsing to a point the object will virialize. The analytic evolution for the top hat density and temperature therefore must be modified to approximate the virial behaviour. Tegmark et al. (1997) modeled the formation of primordial objects with a semi-analytic approach. They assumed that the density followed the top hat solution until the temperature reached the virial value, after which the density remained constant at  $18\pi^2$  times the background density at the nominal collapse redshift. If the overdensity reached the virial value before  $T > T_{vir}$ , they held the density constant and assumed that the gas would be shock heated to the virial temperature. This density function, the cooling rate, and chemical reactions were integrated to follow the temperature and chemical abundances in the top hat.

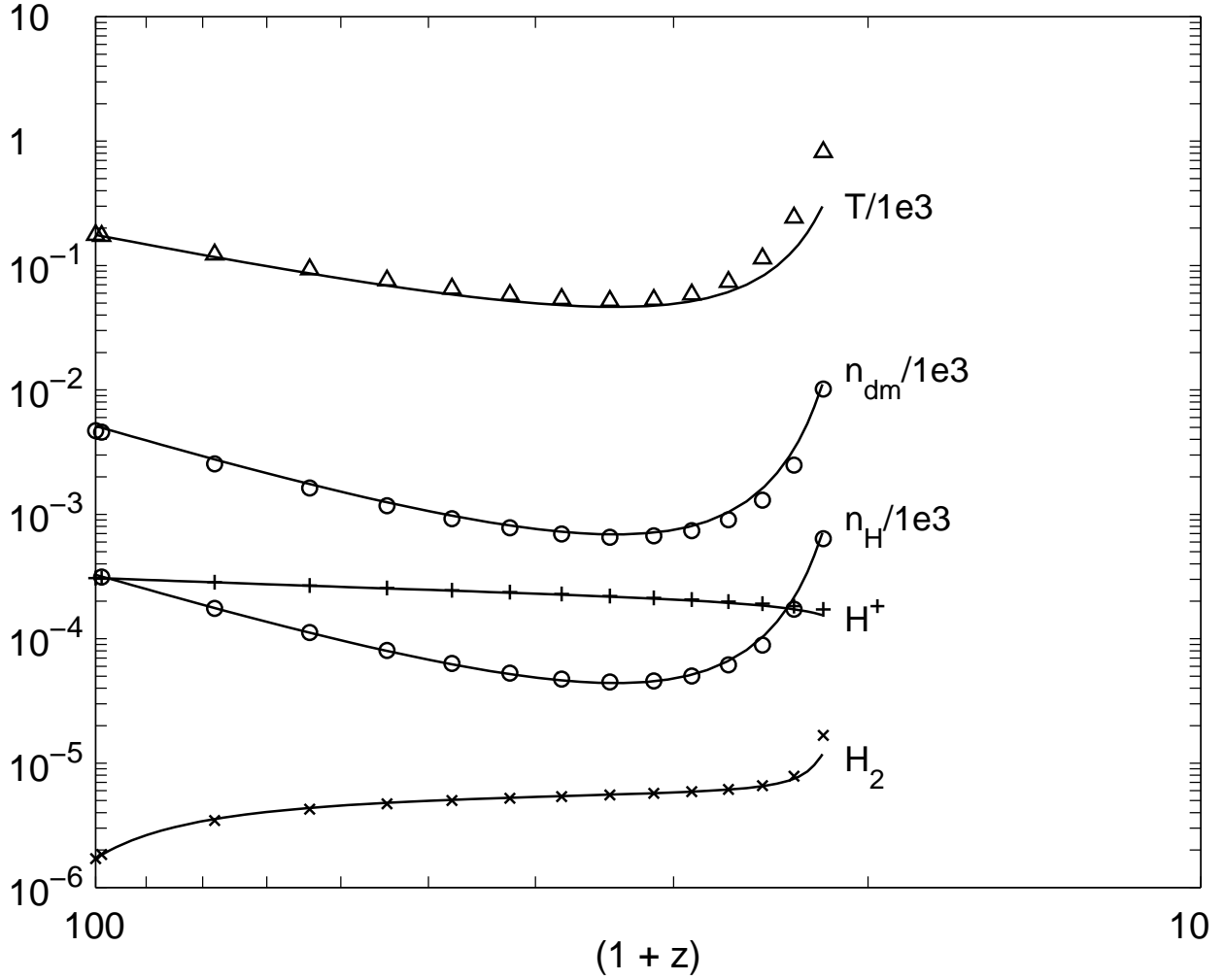


Fig. 6.— Comparison of temperatures, baryonic and dark matter densities,  $H^+$ , and  $H_2$  fractions given by an analytic top hat model (solid lines) and our  $N$ -body code, Hydra (symbols) for a perturbation of total mass  $10^6 M_\odot$  that virializes at  $1+z=20$ .

Many cosmological simulations use a regular cubic lattice for the initial particle distribution, onto which is imposed a power spectrum of fluctuations according to the cosmology. For a simple top hat model, the only fluctuation imposed is a simple compression of a spherical region of space. A cubic grid is inappropriate in this case since collisionless particles would collapse to a singularity and oscillate about the collapse centre. We introduce noise into the particle distribution in order to generate substructure which will lead to virialization.

To make a fair comparison between the semi-analytic top hat model and the simulations, the initial conditions must be set up to mimic the semi-analytic behaviour as closely as possible. This however involves two antagonistic criteria. Very smooth initial conditions will not produce as much substructure and will follow the semi-analytic top hat model closely up to the virialization redshift. However, the smooth initial conditions do not allow the dark matter to virialize well: much of the dark matter rebounds outward to a large distance while also producing a very dense, small virialized region which has an overdensity well above the semi-analytic value of  $\delta \simeq 200$ . Adding more noise to the initial conditions promotes the formation of substructure which results in a larger portion of the dark matter contained in the virialized region and a smaller central overdensity, but the increased substructure causes the temperature and density to rise slightly above the semi-analytic value prior to virialization.

The amount of substructure that forms before the dark matter virializes is governed by the noise in the initial particle positions and the time elapsed between the start of the simulation and virialization. Without altering the initial particle positions, substructure in the dark matter may be quantitatively increased by simply starting the simulation at an earlier redshift. One must now decide upon an appropriate amount of substructure to use. We have chosen to use random initial conditions and start the simulations at a redshift that is 20 expansion times prior to virialization (eg.  $z_i = 400$  for  $z_v = 20$ ; these values are appropriate for a top hat containing roughly  $10^4$  particles). This arrangement produces a virialized region with approximately 80% of the dark matter within the analytic virial radius, and a mean overdensity within the half-mass radius of approximately 200. This creates post-virialization conditions that are similar to the semi-analytic model, at the expense of pre-virialization agreement. Baryons will fall into the shallow potential wells provided by the substructure present in the dark matter, slightly elevating the density, temperature, and  $H_2$  abundance. The amount of disagreement with the semi analytic model prior to virialization is small and has negligible impact upon the post-virialization behaviour. Requiring the presence of substructure is also attractive since this reflects more closely collapses in a hierarchical CDM cosmology — they are never monolithic, as they are in the analytic top hat model.

We performed several top hat runs and compared with the semi-analytic predictions. We find that after virialization, for objects that remain pressure supported, the simulations agree well with the semi-analytic model because the baryon overdensity remains near the virial value. For objects that are able to cool and become self gravitating, the baryon overdensities become much higher than the virial value, and the semi-analytic model does not agree well with the simulations. However, if the post-virialization baryon density in the semi-analytic model was raised to the value observed

in the simulations, the chemical abundances and temperature agreed very well.

### 3.2. Sensitivity to initial chemical abundances

The  $\text{H}_2$  abundance in the early Universe has been computed by many authors and varies considerably:  $\approx 10^{-4}$  (Tegmark et al. 1997; Haiman et al. 1996),  $5 \times 10^{-7}$  (Lepp & Shull 1983),  $7.5 \times 10^{-6}$  (Puy et al. 1993). The simulations performed here use the  $\text{H}_2$  abundance given by Anninos & Norman (1996):

$$f_{\text{H}_2} = 2 \times 10^{-20} \frac{f_{\text{H}} \Omega_0^{3/2}}{h \Omega_B} (1 + z_0)^{5.1} \quad (12)$$

where  $z_0$  is the largest redshift at which  $\text{H}_2$  can be efficiently formed through the  $\text{H}_2^+$  channel. Peebles (1993) found the residual ionization after recombination to be:

$$f_{\text{H}^+} = 1.2 \times 10^{-5} \Omega^{1/2} / (h \Omega_B). \quad (13)$$

To determine the sensitivity that the initial  $\text{H}_2$  abundance has on the collapse, two  $N$ -body simulations of top hat perturbations were run with initial  $\text{H}_2$  abundances of  $2 \times 10^{-6}$  and  $\sim 10^{-4}$ . Figure 7 shows the evolution of the baryonic and dark matter densities, the temperature, and the  $\text{H}_2$  and  $\text{H}^+$  abundances for the central region of a top hat with  $M = 10^6 M_\odot$  that virializes at  $1 + z_v = 20$ . The  $\text{H}_2$  abundance for  $z \leq z_v$  is not sufficient in either run to alter the gas temperature and hence the gas evolves adiabatically: it cools with the expansion up to the turnaround redshift  $z_t = 30$  and subsequently heats as the perturbation begins to contract. After turnaround the increase in baryonic density accelerates the molecular hydrogen production and the difference in the  $\text{H}_2$  abundances between the two runs quickly disappears. Both runs reach the same final value of  $f_{\text{H}_2} = 10^{-3}$  shortly after virialization. Another run was done using an initial  $\text{H}_2$  abundance of  $10^{-8}$  which shortly stabilized at  $f_{\text{H}_2} = 5 \times 10^{-6}$ . Prior to virialization, there are no reactions that efficiently destroy  $\text{H}_2$ , and the factor limiting the  $\text{H}_2$  abundance is the number of free electrons available to catalyze the  $\text{H}^-$  channel. The temperature, density, and chemical evolution after virialization are thus insensitive to the initial molecular hydrogen abundance.

The molecular hydrogen abundance reaches a plateau before virialization of  $6 \times 10^{-6}$  which disagrees with the simulations of Haiman et al. (1996) and Tegmark et al. (1997) who found the plateau values to be  $1.6 \times 10^{-4}$  and  $10^{-4}$  respectively. These authors have used a rate for the photodissociation of  $\text{H}_2^+$  (important at  $z > 200$ ) that is too low, which consequently caused a higher  $\text{H}_2$  abundance, as noted by Abel et al. (1998). Our  $\text{H}_2$  abundance agrees with the newer calculations of Galli & Palla (1998) and Abel et al. (1998).

Regardless of the redshift at which the simulations are started, the chemical abundances are initialized at  $z = 100$  and from then on the chemical reactions and cooling processes are followed. Computing the abundance of  $\text{H}_2$  at earlier redshifts necessitates inclusion of more chemical reaction which would slow the code, only to produce an  $\text{H}_2$  abundance at  $z = 100$  which is already known

(see e.g. Galli & Palla 1998). At this redshift, the top hat simulations are still quite smooth and the baryonic density and temperature are not significantly different from the background values. Some error in the initial abundances is undoubtedly committed by neglecting to compute the chemistry at redshifts earlier than 100, but as shown above, variations in the initial  $\text{H}_2$  abundance do not alter the post-virialization behaviour.

### 3.3. Softening issues

In order to avoid excessively large forces between two particles in close proximity, the gravitational attraction is “softened” so that the gravitational force decreases at small distances. The distance at which the softened gravity diverges from the Newtonian value is set by the softening length,  $s$ . This parameter must be carefully tuned to the problem, otherwise the results will be tainted by unphysical numerical effects. If  $s$  is too small then two body collisions become apparent; if  $s$  is too large then the softening may prevent a group of particles from reaching a density high enough to correctly model a self-gravitating region — a necessary condition for star formation. SPH forces are computed by using a smoothing kernel to average over the approximately 32 nearest neighbours; the SPH smoothing length ( $h$ ) is chosen adaptively such that it encloses that number of neighbours. In very dense regions, however, it is necessary to constrain the SPH smoothing length to a minimum value (one half of the gravitational softening length) to balance the gravitational and hydrodynamic resolutions, otherwise unphysical clustering of the baryon particles can occur (Thacker et al. 1998). The minimum smoothing length determines the maximum density that the gas particles may reach. Efficient cooling leads to dense clustering of the baryons relative to the dark matter particles, and a mismatch in the ideal  $s$  and  $h_{min}$ . We have performed several tests to quantify the effects that different softening and smoothing lengths produce.

The overdensity of an object in which gas pressure is initially unimportant is, at virialization,  $1 + \delta = 18\pi^2$  in an  $\Omega = 1$  universe (Gunn & Gott 1972). The mean separation between particles in the perturbation is then  $d = (18\pi^2)^{-1/3} d_{bg}$  where  $d_{bg}$  is the mean interparticle separation of the uniform background matter. For a simulation box volume of  $V = L^3$  containing  $N = n^3$  particles,  $d_{bg} = L/n$  and  $d \simeq 0.2L/n$ . The softening length should enclose at least roughly 10 particles to minimize spurious two body effects, which gives  $s = 2d \simeq 0.4L/n$ . This may be taken as an estimate of the minimum softening length, since the central region of a virialized object has an overdensity well in excess of  $\delta \simeq 200$ . As an extreme, if  $\delta = 10^5$ , then  $s \simeq 0.04L/n$ .

The smoothing length has a much greater effect on the baryonic density than on the dark matter density for cases in which the baryons can cool efficiently. This is illustrated in figure 8 which shows the baryonic and dark matter density profiles for top hat simulations using various smoothing lengths (table 2, runs 1 to 4). In these runs, enough  $\text{H}_2$  is formed that the gas can cool efficiently and free fall into the dark matter potential well. If  $s$  is too large, then the baryonic density  $\rho_b$  remains lower than the dark matter density  $\rho_{DM}$ . The smoothing length has the undesirable ability to determine if the gas can become self gravitating (i.e.  $\rho_b \geq \rho_{DM}$ ). This problem does not

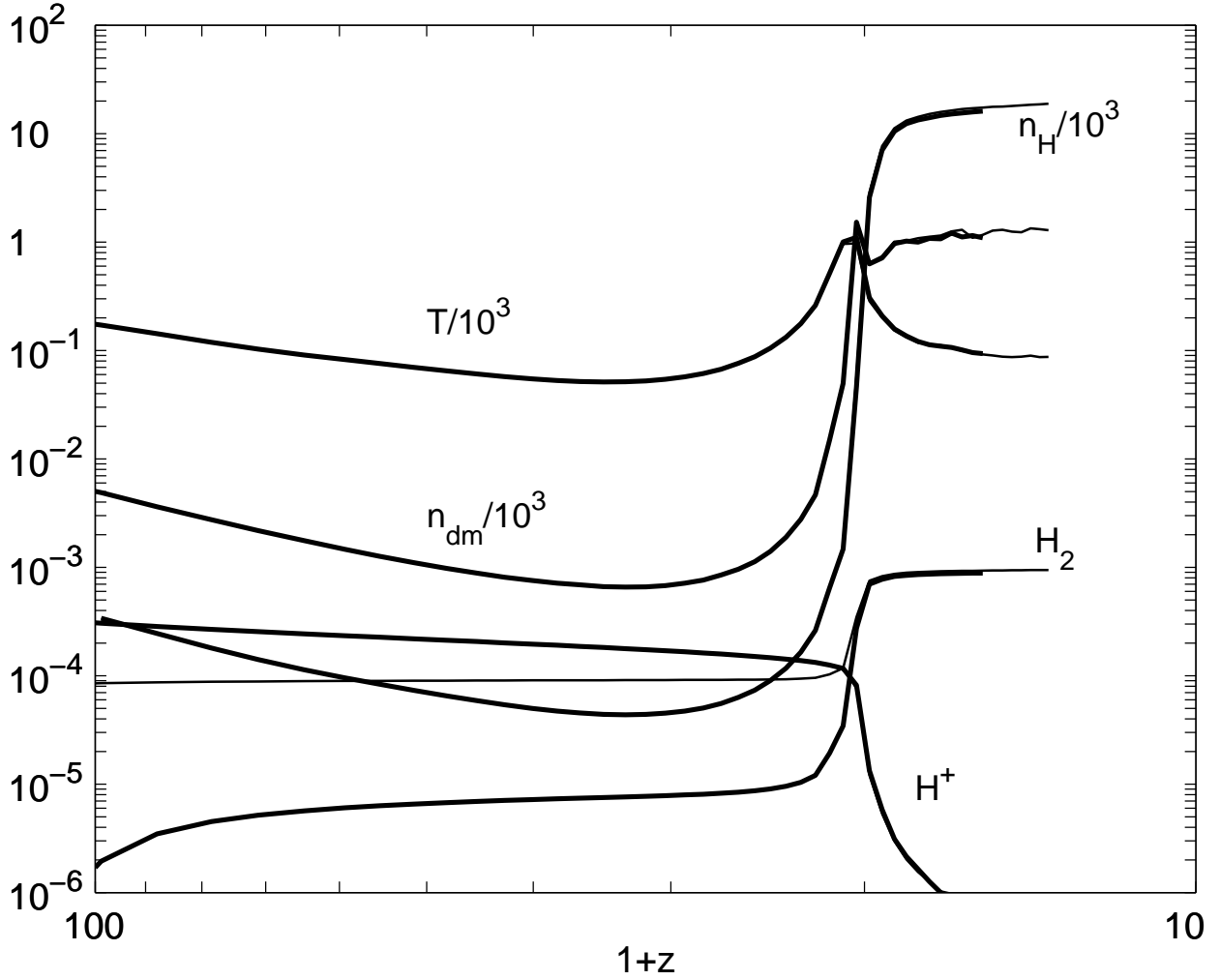


Fig. 7.— A comparison of two runs having initial molecular hydrogen abundances of  $2 \times 10^{-6}$  (thick lines) and  $\sim 10^{-4}$  (thin lines). The final physical and chemical states of the object after virialization ( $z = 20$ ) are insensitive to the initial  $\text{H}_2$  abundance.

exist for hot, pressure supported objects — in these, even an extremely small softening will not cause the object to become self-gravitating (figure 9).

Since we are concerned with finding the minimum mass of an object that can cool efficiently and become self-gravitating, the situation above where the softening has such a strong influence on the baryonic density is unsatisfactory. A collapse criterion sensitive to numerical (*not* physical) parameters is not robust. In a pressure-supported object, the number of particles within the softening radius is approximately 32, while in a self gravitating object the number of particles will be magnitudes larger. Figures 10 and 11 show the mass and temperature profiles for an object that has cooled and an object that is pressure supported. The number of particles (and also mass and temperature) within the softening radius of an object that has cooled stays fairly constant regardless of the size of the softening radius. As an alternative to the comparison between  $\rho_b$  and  $\rho_{DM}$  comparison, we consider an object to be have collapsed to a self gravitating state if there are more than one thousand particles within the softening radius at a temperature of just over 100 K. In practice it is quite easy to distinguish between objects that have become self gravitating and those that are pressure supported since the former display rapid and obvious changes in their density and temperature profiles.

### 3.4. Particle resolution

Increasing the number of particles in an  $N$ -body simulation provides better resolution, at the expense of computational speed. Since we intended to perform many simulations of top hat perturbations of different masses and virialization redshifts in order to determine the mass required for an object to become self gravitating at a certain redshift, it was desirable to find the minimum number of particles that would provide acceptable resolution. This minimum number will also provide a pointer to the particle mass resolution necessary for robust simulations of the first objects in a cosmological setting.

We performed several simulations using various particle resolutions, and found that the central density in  $N = 2 \times 16^3$  runs was lower than that in  $N = 2 \times 32^3$  runs. Some variation with resolution has to be expected since the central regions in the lower resolution runs are marginally resolved. In objects where the central gas cools quickly, within the softening radius there are about 50 dark matter and 500 gas particles in the  $2 \times 16^3$  simulations. The  $2 \times 32^3$  runs have well defined cores containing approximately 600 dark matter and 6000 gas particles within the softening radius. Throughout the paper we will use the term “core” to describe the regions in self gravitating objects that have constant (with respect to distance to centre) high density and low temperature.

The  $N = 2 \times 32^3$  runs in which the gas is able to cool efficiently have  $N_{gas}(r)$  (cumulative number of gas particles) profiles that are flat, which indicates that almost all of the gas particles initially contained in the top hat perturbation lie within the softening radius. In this case the resolution is limited by the softening length and not the number of particles, but for the  $N = 2 \times 16^3$

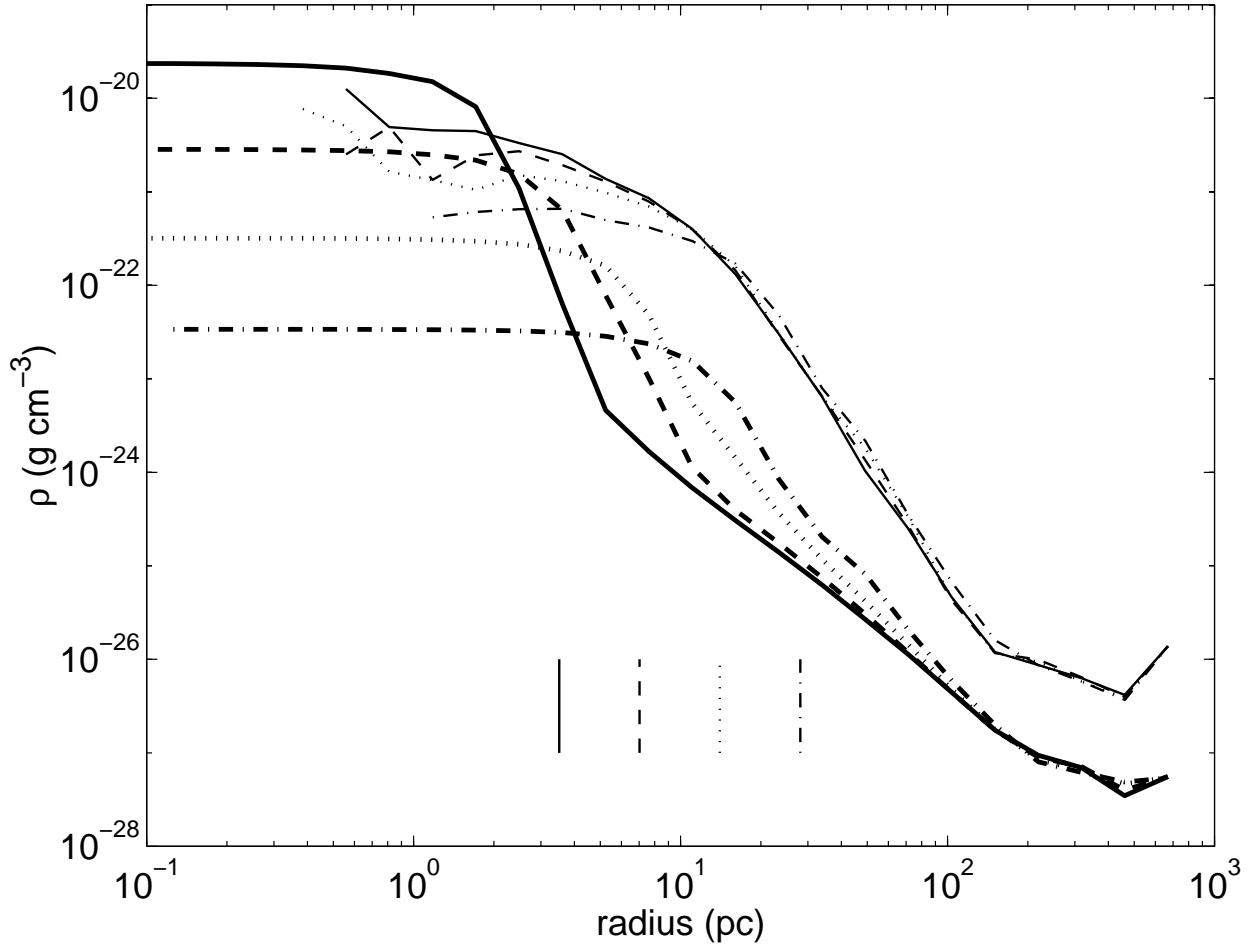


Fig. 8.— Density profiles of an object that can cool efficiently (runs 1 to 4) for various softening lengths. Shown are the dark matter density (thin lines — computed dividing the mass in a radial shell by its volume), and the baryon density (thick lines — computed by averaging the SPH density of all particles within a radial shell). The vertical lines show the softening lengths used for each simulation. The runs with the two smallest softening values have self-gravitating cores ( $\rho_b > \rho_{DM}$ ). Increasing the softening further causes the baryonic density to drop below that of the dark matter density.



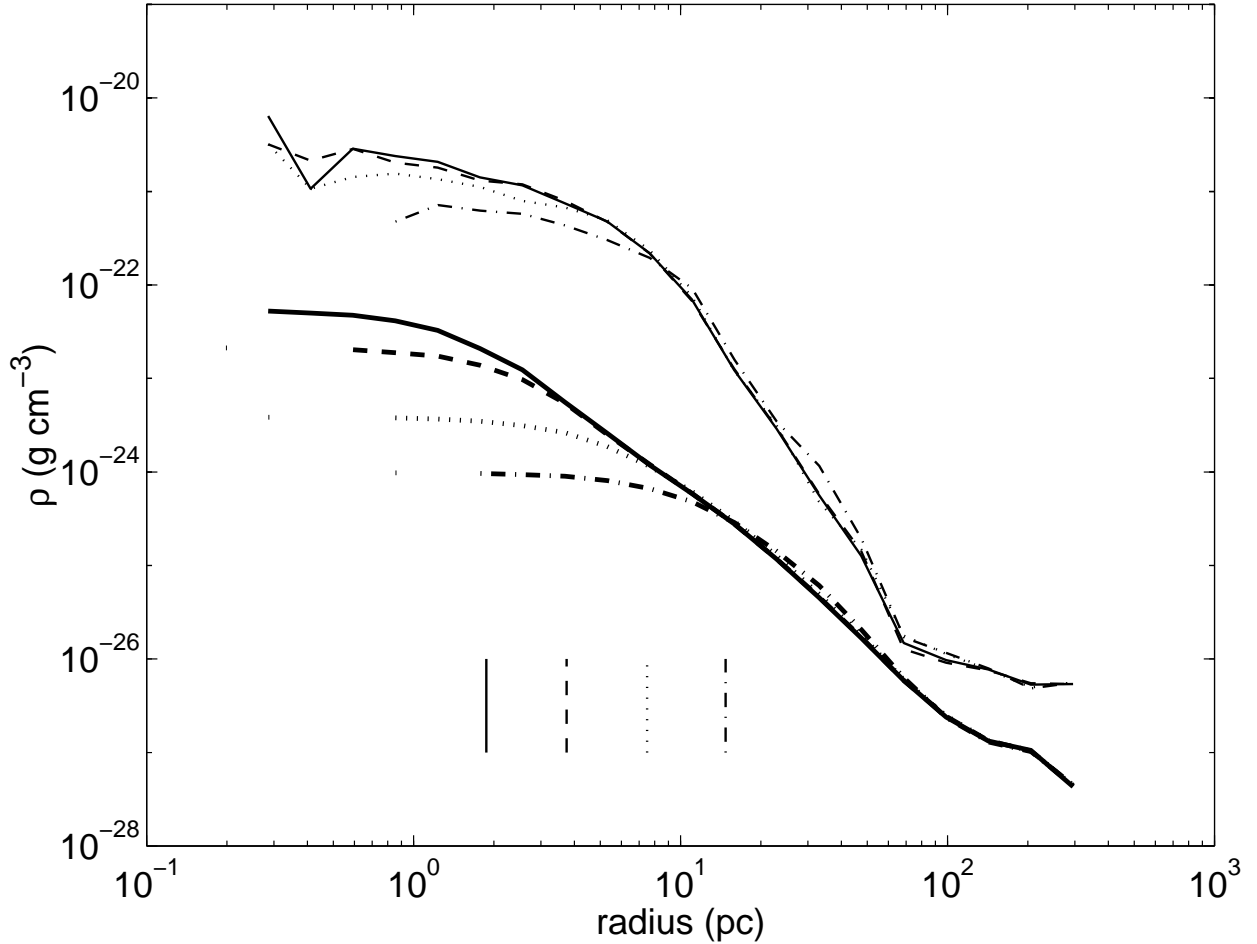


Fig. 9.— Density profiles of a pressure supported object (runs 5 to 8) for various softening lengths. In the pressure supported case, softening does not determine if the central region becomes self-gravitating ( $\rho_b > \rho_{DM}$ ). As in figure 8, thick lines are baryon densities and the thin lines are dark matter densities. The vertical lines show the softening lengths used for each simulation. Densities beyond the softening length are convergent with densities computed using a smaller softening length.

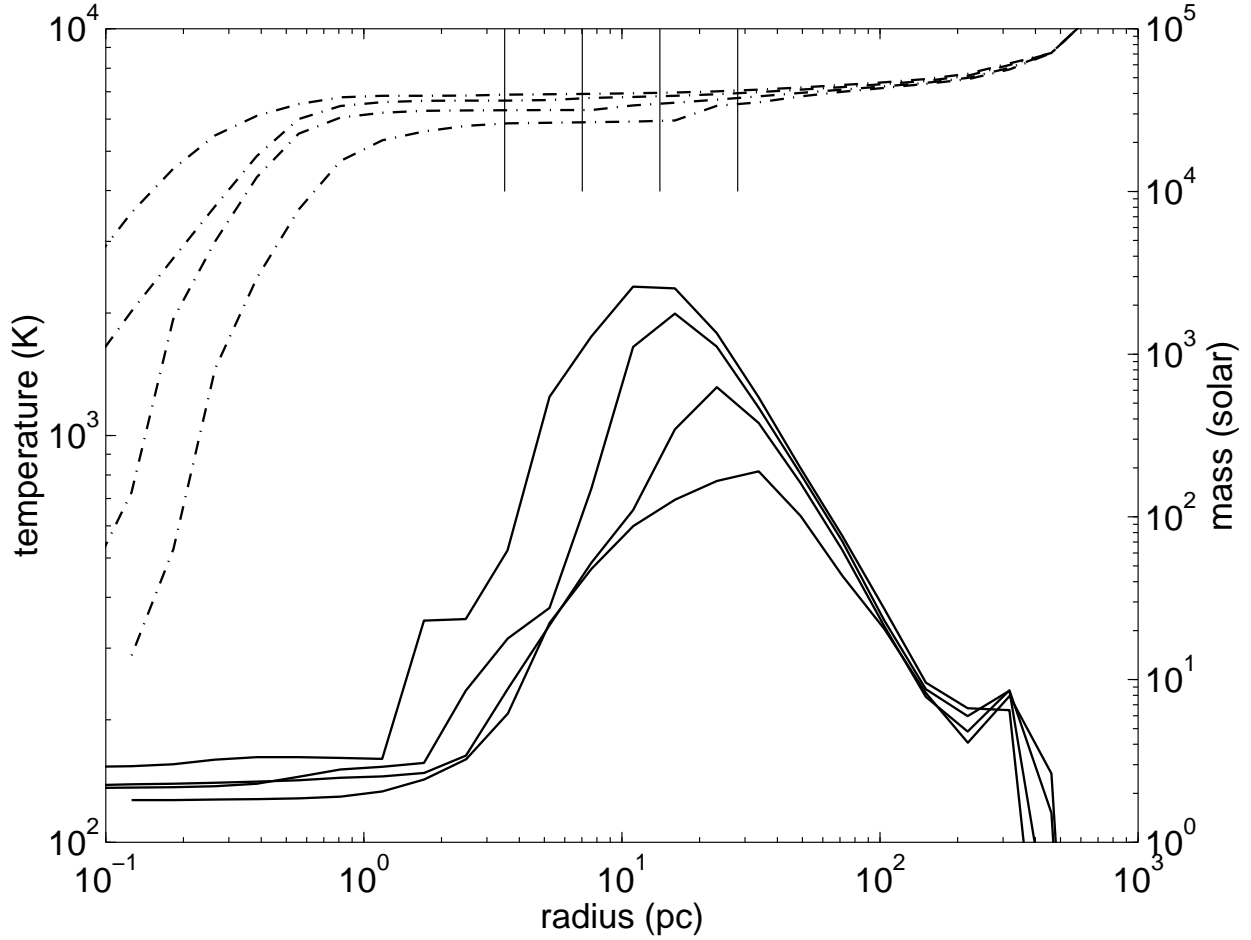


Fig. 10.— Radial profiles of gas temperature (solid lines) and gas mass (broken lines) for various smoothing lengths (runs 1 to 4). The object contains about 9000 particles, has a total mass of  $10^6 M_{\odot}$  and is able to cool efficiently. As the smoothing length (vertical lines) is increased the peak temperature decreases, but the temperature of the baryons in the core of the object ( $r \lesssim 1\text{pc}$ ) is not significantly influenced by the smoothing length. There are approximately 3000 gas particles within the smoothing length regardless of its value, and they have cooled to a temperature where  $\text{H}_2$  is no longer an effective coolant.

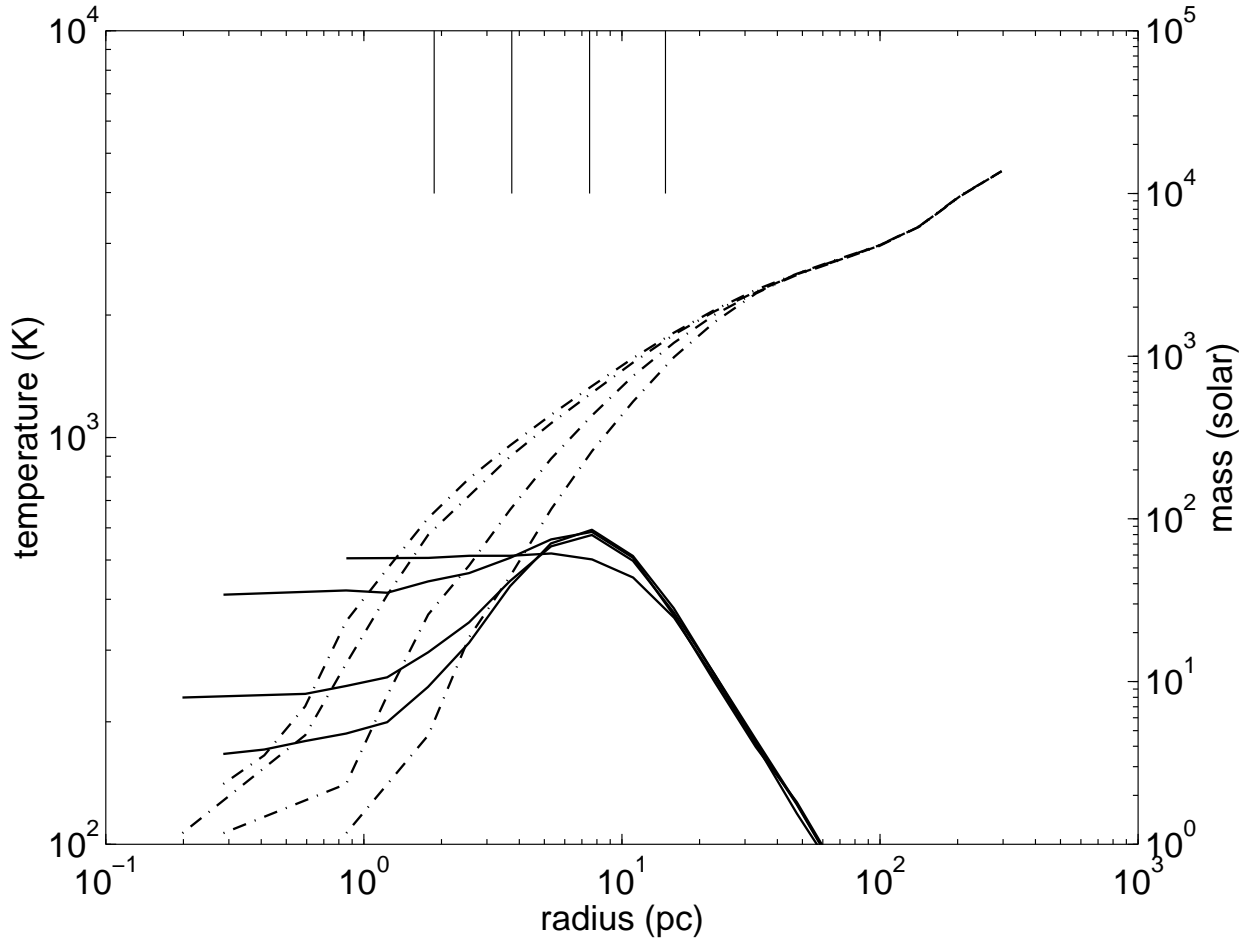


Fig. 11.— Radial profiles of gas temperature (solid lines) and gas mass (broken lines) for various smoothing lengths (runs 5 to 8) for an object of total mass of  $2 \times 10^5 M_{\odot}$  which is not able to cool efficiently. As the smoothing length is decreased (vertical lines), the central temperature decreases and approaches the central temperature observed in an object that is able to cool efficiently (fig. 10), however the central density is very much less for pressure supported objects.

run the situation is reversed. This demonstrates that the minimum limit of acceptable particle resolution has been reached. We performed one top hat simulation with  $N = 2 \times 64^3$  and found the results agreed with the  $N = 2 \times 32^3$  run and are confident therefore that  $2 \times 32^3$  particles provide adequate resolution.

The dark matter alone drives the gas dynamics until the baryonic material becomes self gravitating. The differences in the distribution in the baryonic matter between the  $N = 2 \times 16^3$  and  $N = 2 \times 32^3$  simulations is primarily caused by the differences in the dark matter distribution. The mass profiles in the  $N = 2 \times 32^3$  runs were close to  $M(r) \propto r^3$  as expected for a perturbation of uniform density, but in the  $N = 2 \times 16^3$  runs there simply are not enough particles to accurately model the smooth density of the top hat model, and the mass profiles deviate from being proportional to volume.

Table 2. Simulation parameters for softening and resolution tests

run	mass ( $10^6 M_\odot$ )	box size (kpc)	softening (pc)	$z_v$	N
1	1.03	20.8	3.5	20	$2 \times 32^3$
2	1.03	20.8	7.0	20	$2 \times 32^3$
3	1.03	20.8	14.0	20	$2 \times 32^3$
4	1.03	20.8	28.0	20	$2 \times 32^3$
5	0.17	11.4	1.9	20	$2 \times 32^3$
6	0.17	11.4	3.7	20	$2 \times 32^3$
7	0.17	11.4	7.5	20	$2 \times 32^3$
8	0.17	11.4	14.7	20	$2 \times 32^3$

#### 4. Determination of minimum mass threshold for baryonic condensation

In CDM-like cosmologies, smaller dark matter perturbations collapse at higher redshifts, but for the baryonic matter to become self gravitating, enough  $\text{H}_2$  must exist for the gas to be able to cool efficiently. The rate of  $\text{H}_2$  formation is related to the baryonic density which is initially driven by the dark matter potential well. A minimum mass exists above which the  $\text{H}_2$  production rate is sufficient to cool the gas efficiently. This mass threshold is a function of redshift, and in this section we explore this parameter space by simulating top hat perturbations of various masses. Our main interest is to perform more realistic cosmological simulations of primordial object formation, and the analytic and top hat simulations provide a reasonable estimate of the mass scale at which collapse should occur at a given redshift. All simulations presented here are in an Einstein-de Sitter universe with  $\Omega_{dm} = 0.94$ ,  $\Omega_b = 0.06$ , and a Hubble constant of  $H_0 = 65 \text{ km s}^{-1} \text{ Mpc}^{-1}$ .

An object must contain a certain mass of dark matter to be able to force the baryons into a self gravitating state where star formation may begin. This mass is redshift dependent: as the universe expands it becomes less dense, and deeper dark matter gravitational potential wells are required to drive up the baryonic density to a point where  $\text{H}_2$  production becomes efficient enough that the object may cool on a dynamical time. In this section, using both the semi-analytic and  $N$ -body methods, we have determined the minimum mass required for the baryons in an object to become self gravitating ( $M_{SG}$ ) as a function of redshift.

Figure 12 shows the minimum mass threshold versus redshift relation originally computed by Tegmark et al. (1997). Using the same method, our result differs considerably since we have used a different molecular hydrogen cooling function (see fig. 2), and have included different chemical reactions. Tegmark et al. (1997) used the cooling function of Hollenbach & McKee (1979), and assumed that the  $\text{H}_2$  molecules are all in the para state and that  $\text{H}_2$  vibrational cooling was negligible. At temperatures higher than 1000 K,  $\text{H}_2$  vibrations may be excited and vibrational cooling becomes important; this is why the cooling function that Tegmark et al. (1997) used drops below the other curves when  $T > 1000 \text{ K}$ . More efficient cooling allows smaller, less dense objects to collapse, and consequently our computation of  $M_{SG}(z)$  is a factor of approximately 3 smaller at  $z = 50$ . At  $z = 10$ , Tegmark et al. (1997) found that the objects able to cool efficiently had temperatures of approximately  $10^4 \text{ K}$ , and at this temperature their cooling function is two orders of magnitude lower than the cooling function we used. Also, at temperatures greater than  $10^4 \text{ K}$   $\text{H}_2$  dissociation reactions become important. Since they did not incorporate any  $\text{H}_2$  destruction mechanisms their  $\text{H}_2$  abundances are too high, though this is not enough to offset the less efficient cooling function. We find that objects able to cool efficiently at  $z = 10$  are 25 times less massive.

The results of several  $N = 2 \times 32^3$  top hat simulations are also shown for comparison with the analytic model (fig. 12). Inside the top hat there are  $\simeq 2 \times 10^4$  particles, and in cases where gas in the central region cools quickly, the condensed cores are well resolved and contain  $\simeq 4 \times 10^3$  particles. For a top hat of total initial mass  $M_{TH}$  destined to virialize at  $z = z_v$ , we have plotted a star if the collapse succeeded (using the collapse criterion developed in section 3.3) within one

dynamical time after virialization and a circle if the object remained pressure supported. Some disagreement between the simulations and the semi-analytic result is to be expected since the latter assumes that the baryonic overdensity remains constant at  $\delta = 200$  after virialization, and is uniform within the top hat. In spite of the assumptions made in the semi-analytic result and the different criteria used to determine if the collapse was successful, the two methods agree to within a factor of 2. The slope of the  $M_{SG}(z)$  line determined with the semi-analytic method is slightly steeper than for the simulations but we do not consider this difference to be of special significance. Ultimately the precise determination of  $M_{SG}(z)$  is dependent upon the details of the chemical reaction rates and cooling rates, and the amount of substructure present in the object. Further, although the threshold for collapse is very sharp because of the density-cooling feedback (a small increase in mass can cause an appreciable increase in density), the precise position of the line separating collapse from pressure support is highly sensitive to small variations in reaction rates and small numerical changes and hence is simply indicative of the general behaviour in the  $M$ - $z$  plane. Our results show that we expect the collapse mass to be robust within a factor of 2 at a given redshift.

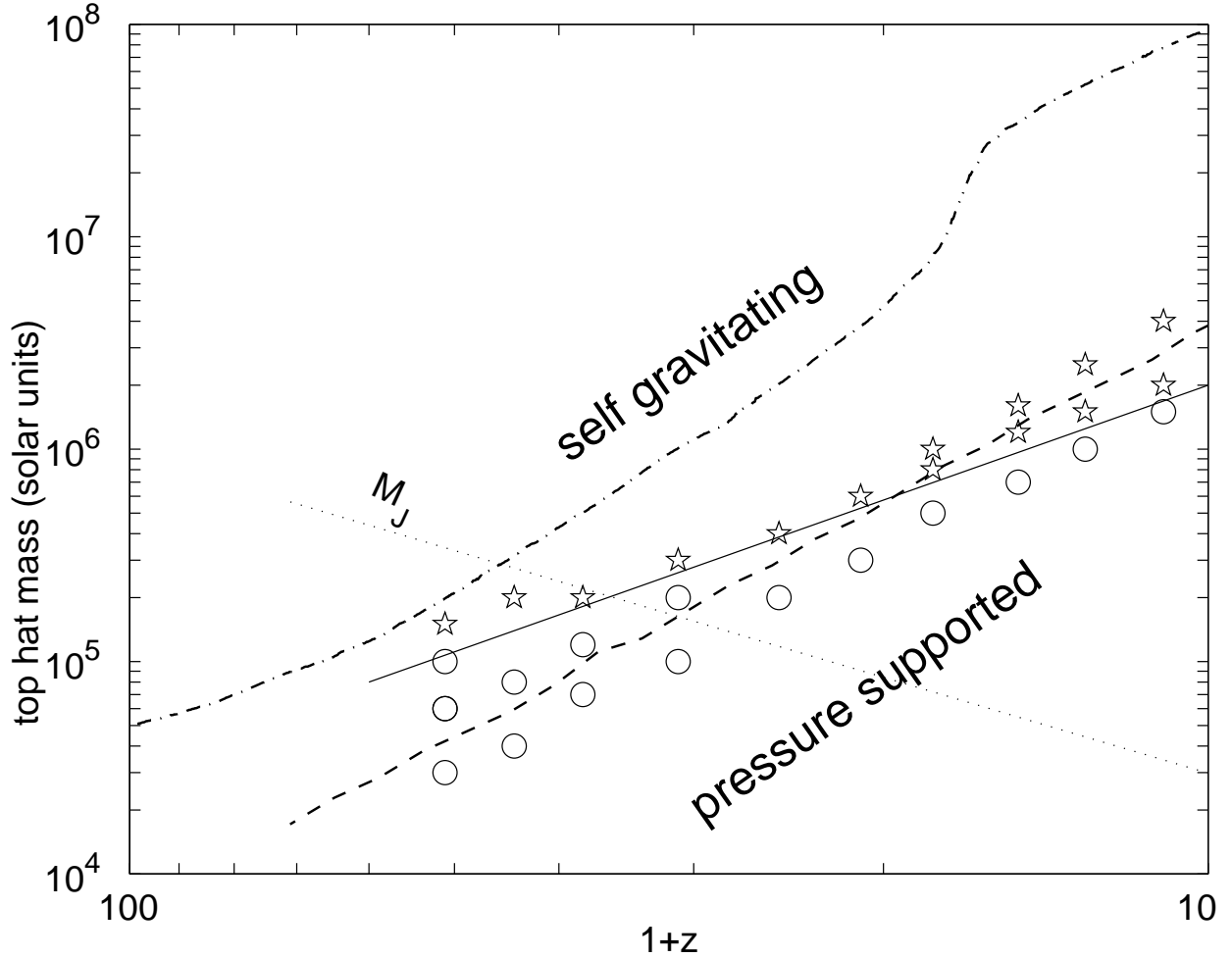


Fig. 12.— Minimum mass threshold required for self gravitation ( $M_{SG}$ ) versus redshift. The dash-dotted line shows the result of Tegmark et al. (1997), and the dashed line shows our semi-analytic result. The dotted line is the Jeans mass. The symbols show results of  $N$ -body simulations using  $2 \times 32^3$  particles. Objects less massive than  $M_{SG}$  at a given redshift will remain pressure supported (circles); more massive objects cool efficiently and the baryonic material in the central region becomes self-gravitating (stars). The solid line is an approximate fit to the simulation results.



## 5. Cosmological simulation of first objects

Our objective here is to follow the growth of objects through merging and accretion in the CDM hierarchy and to be able to identify objects that are able to form enough  $\text{H}_2$  that they cool efficiently and become self gravitating. Of primary interest is the determination of the time at which the object exceeds the Jeans mass threshold, and the time at which the cooling time drops below the dynamical time. To follow objects through these phases we simulated a  $(25h^{-1} \text{ kpc})^3$  volume in an  $\Omega = 3.4$ ,  $\Omega_b/\Omega = 0.06$ ,  $h = 0.65$  universe. An overdense universe was used simply to model the environment of a  $3 - 4\sigma$  perturbation which will lead to the formation of the first cosmological objects. The simulation contained equal numbers of gas and dark matter particles, in total  $N = 2 \times 64^3$ . This gives a mass of  $5.1 M_\odot$  for the baryon particles and  $81 M_\odot$  for the dark matter particles.

The mass evolution and merger history of the most massive object in the simulation is shown in figure 13. We define  $M_{200}$  to be the mass enclosed by a thin shell that has an overdensity of 200. The complete family tree is very large and to reduce the complexity of the plot, at each redshift only the direct ancestors of the most massive object is shown. Lines connect the smaller objects that have merged into the largest object. The separation between the self-gravitating and pressure-supported domains is shown for both the semi-analytic method and the  $N = 2 \times 32^3$  top hat simulations. The agreement between the cosmological simulation and the top hat simulation computation of  $M_{SG}$  is quite good; the point at which the object becomes self gravitating is close to the top hat result.

In Figure 14 we plot the entropy evolution of the approximately 2000 gas particles which reside in the core of the final cooled object. This figure shows clearly the three stages in hierarchical evolution. Before the dark matter halo reaches the Jeans mass, the gas will respond adiabatically to the growing dark matter potential well, and thus the entropy (defined as  $\propto T/\rho^{2/3}$ ) will remain constant at the background value. Once the Jeans mass is reached infalling gas will be shock heated (a non-adiabatic process) and hence will have its entropy raised. Once cooling becomes effective, the entropy in the core drops rapidly.

The baryonic matter in objects less massive than the Jeans mass is pressure supported against gravitational contraction. In these objects the baryonic matter should be relatively unperturbed by the dark matter, and will not have steep baryonic radial density profiles. As the baryonic material in an object approaches the Jeans mass, the baryonic radial density profile will begin to steepen and become similar in shape to the dark matter radial density profile. The most massive object in the simulation exhibits this behaviour, as shown in figure 15. By  $z = 28$  the baryon density profile has started to steepen but its slope is still less than that of the dark matter. At  $z = 24$  the object has exceeded the Jeans mass and the slopes of the baryon and dark matter density profiles become very close.

At  $z = 28$ , the temperature and  $\text{H}_2$  fraction (relative to the total hydrogen abundance) in the most massive object produce a cooling time that is significantly greater than the dynamical time

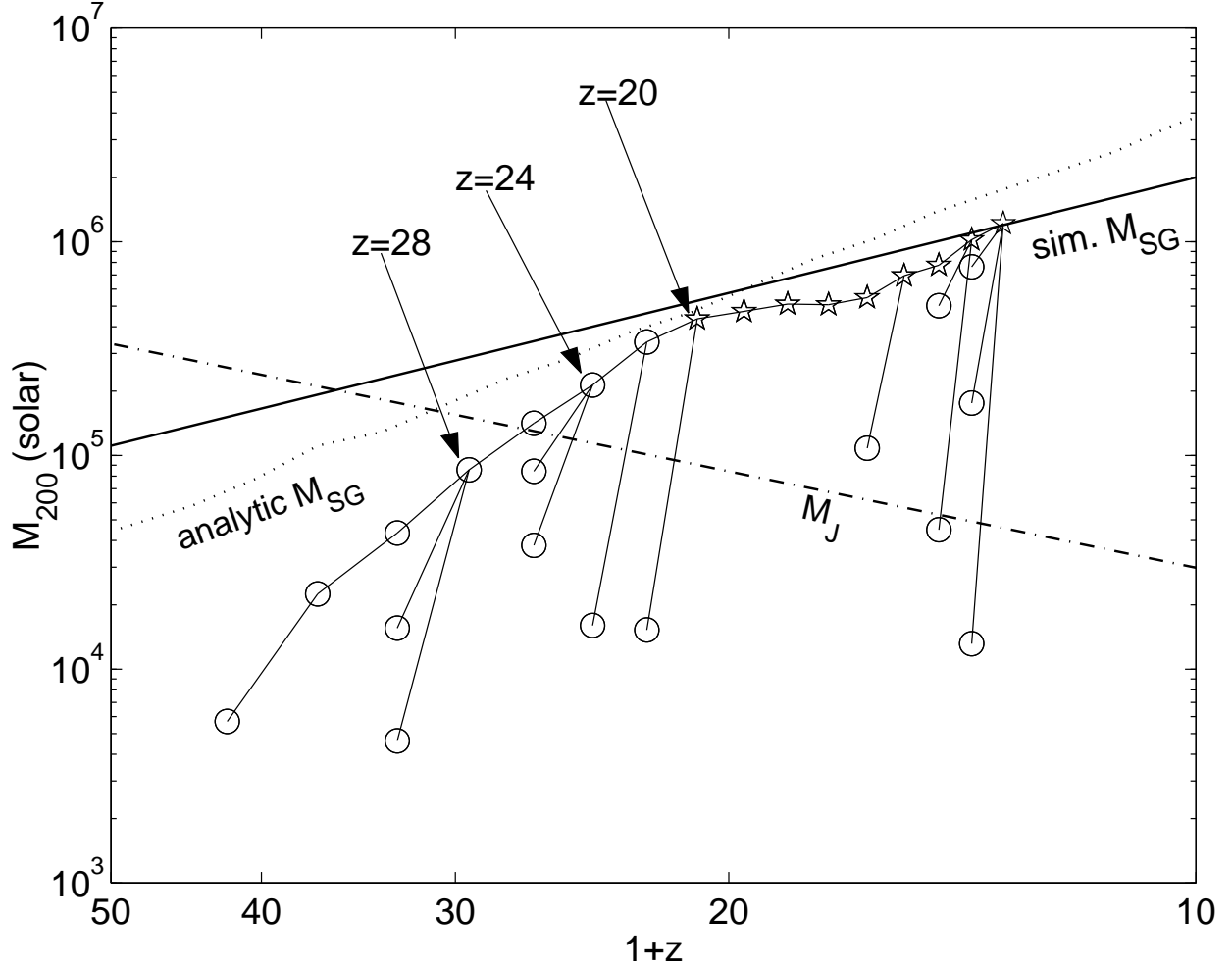


Fig. 13.— The mass evolution and merger history are shown for the most massive object in the cosmological simulation. The thin lines connect objects to their predecessors. The dotted line shows  $M_{SG}$  computed with the semi-analytic method, and the solid line shows the results from the  $N = 2 \times 32^3$  top hat simulations. Initially, the baryonic matter in the objects is pressure supported (circles), and as mass is accreted the gas becomes self gravitating (stars). Physical properties of the indicated objects are shown in figures 15, 16, and 17. Within  $r_{200}$  there are 5100, 2500, and 280 dark matter particles and 4600, 2100, and 160 gas particles at redshifts of 20, 24, and 28 respectively.

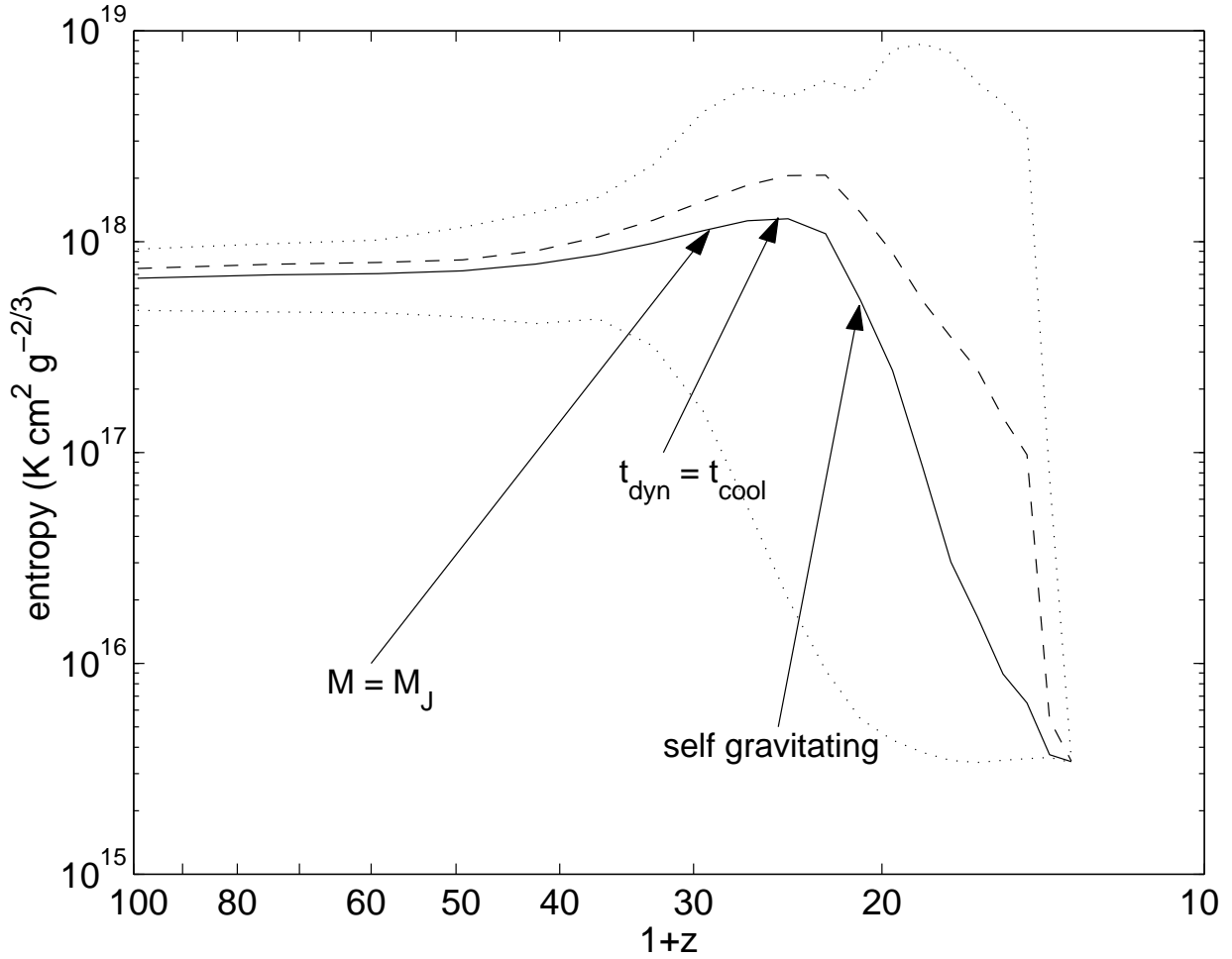


Fig. 14.— The evolution of the entropy of the  $\sim 2000$  core particles in the most massive object in a cosmological simulation. The solid line shows the mean entropy of the core particles, dotted lines show the particles with the minimum and maximum entropy, and the dashed line shows one standard deviation above the mean. Initially the gas is subject to adiabatic processes only, and the entropy does not change with time. As the gas begins to fall into the dark matter potential well and exceeds the Jeans mass, it is shock heated and the entropy begins to rise. After enough  $\text{H}_2$  has formed, the cooling time falls below the dynamical time, rapidly reducing the entropy, and the gas in the core becomes self gravitating within a dynamical time.

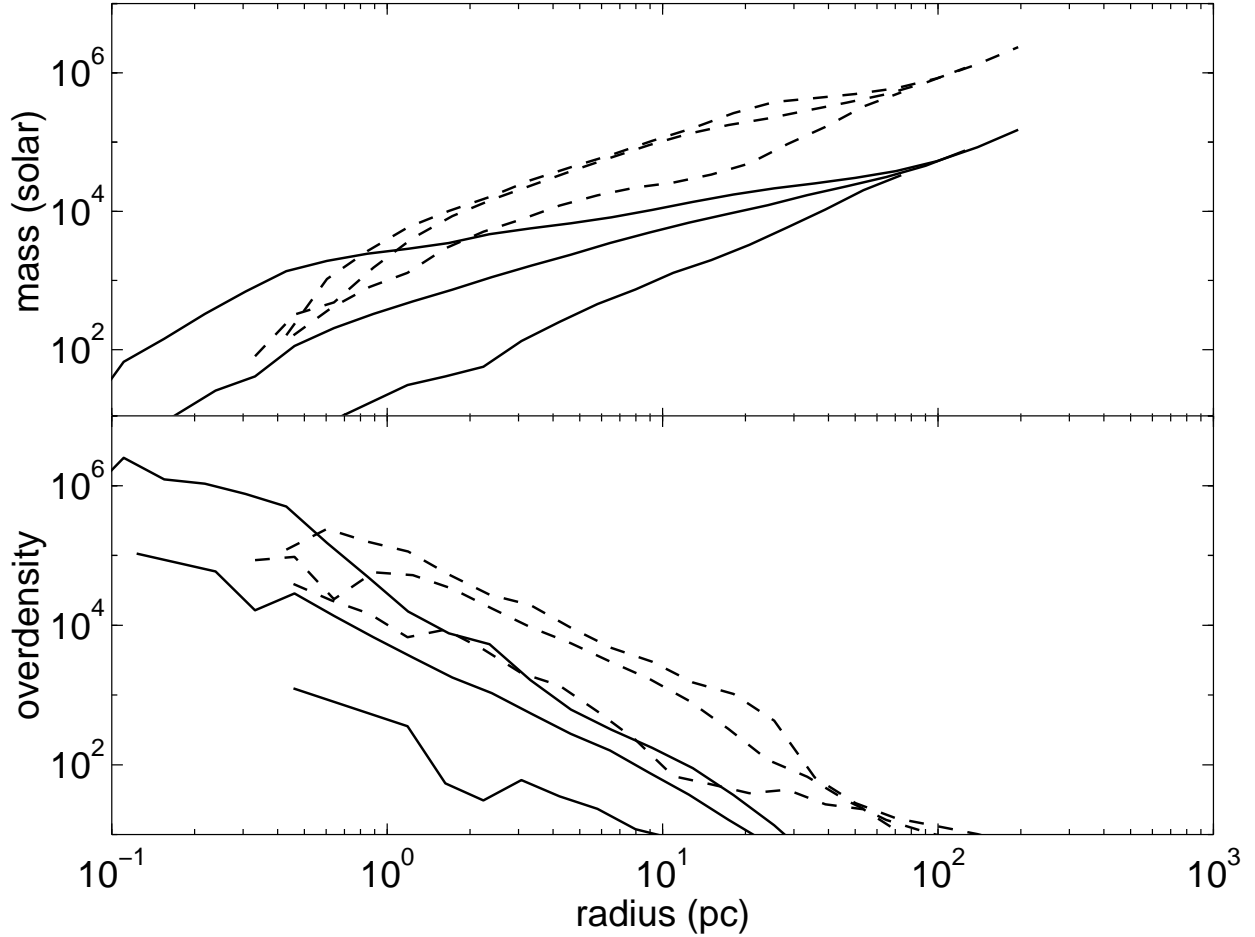


Fig. 15.— The evolution of the radial profiles of the mass and overdensity for baryonic (solid lines) and dark matter (broken lines) are shown for the most massive object in a cosmological simulation at redshifts of 28, 24, and 20. These profiles correspond to the object at the epochs indicated in figure 13. At  $z = 24$  enough  $\text{H}_2$  has formed that the baryons cool efficiently and free fall in the dark matter potential well. By  $z = 20$  —  $10^7$  years or approximately one dynamical time later — the object becomes self gravitating.

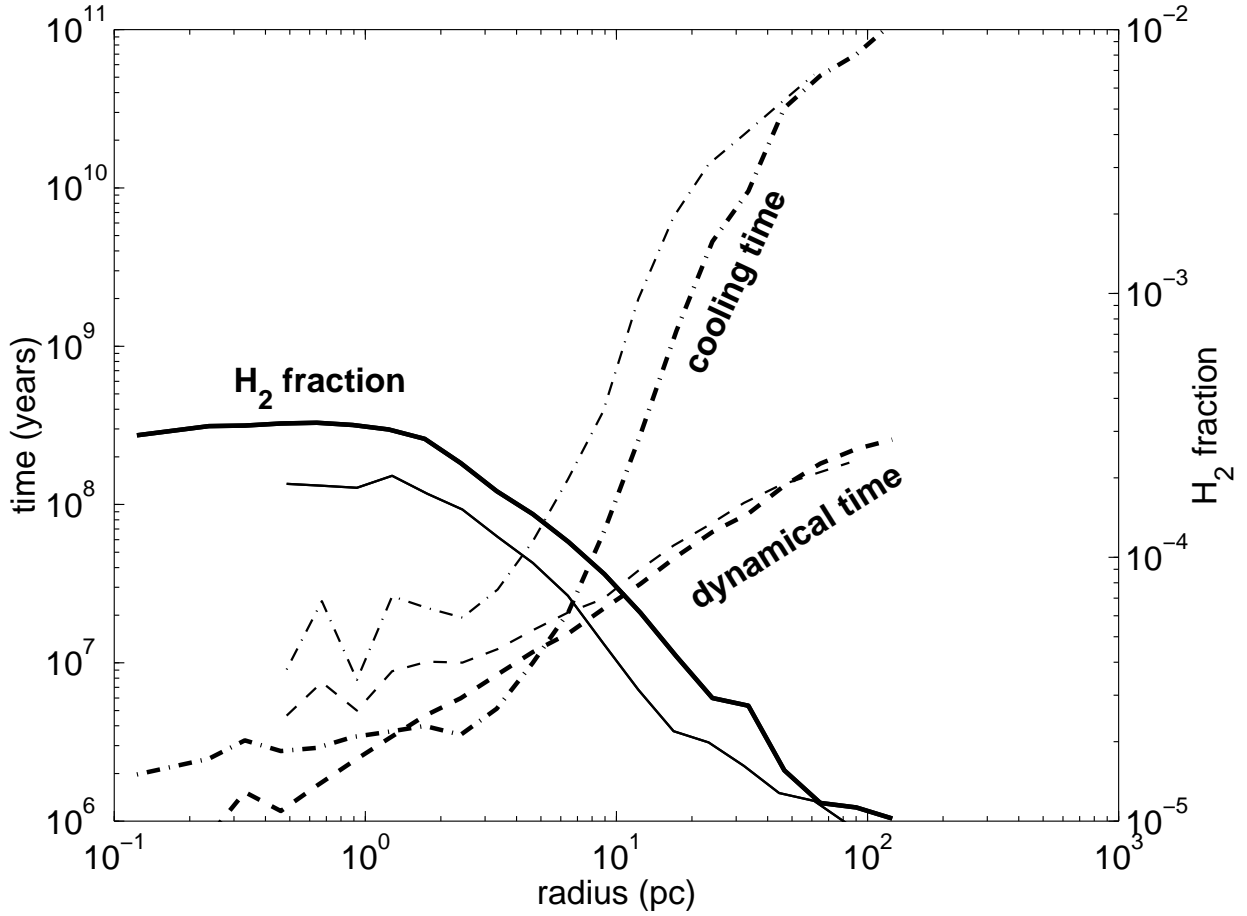


Fig. 16.— The cooling time (dash-dotted lines), dynamical time (dashed lines), and molecular hydrogen fraction (solid lines) are shown at redshifts of 28 (thin lines) and 24 (thick lines) for the most massive object in a cosmological simulation. From  $z = 28$  to  $z = 24$  the increase in density and temperature accelerate the  $H_2$  production. The increase in temperature and  $H_2$  abundance conspire to reduce the cooling time below the dynamical time in part of the central region of the object by  $z = 24$ .

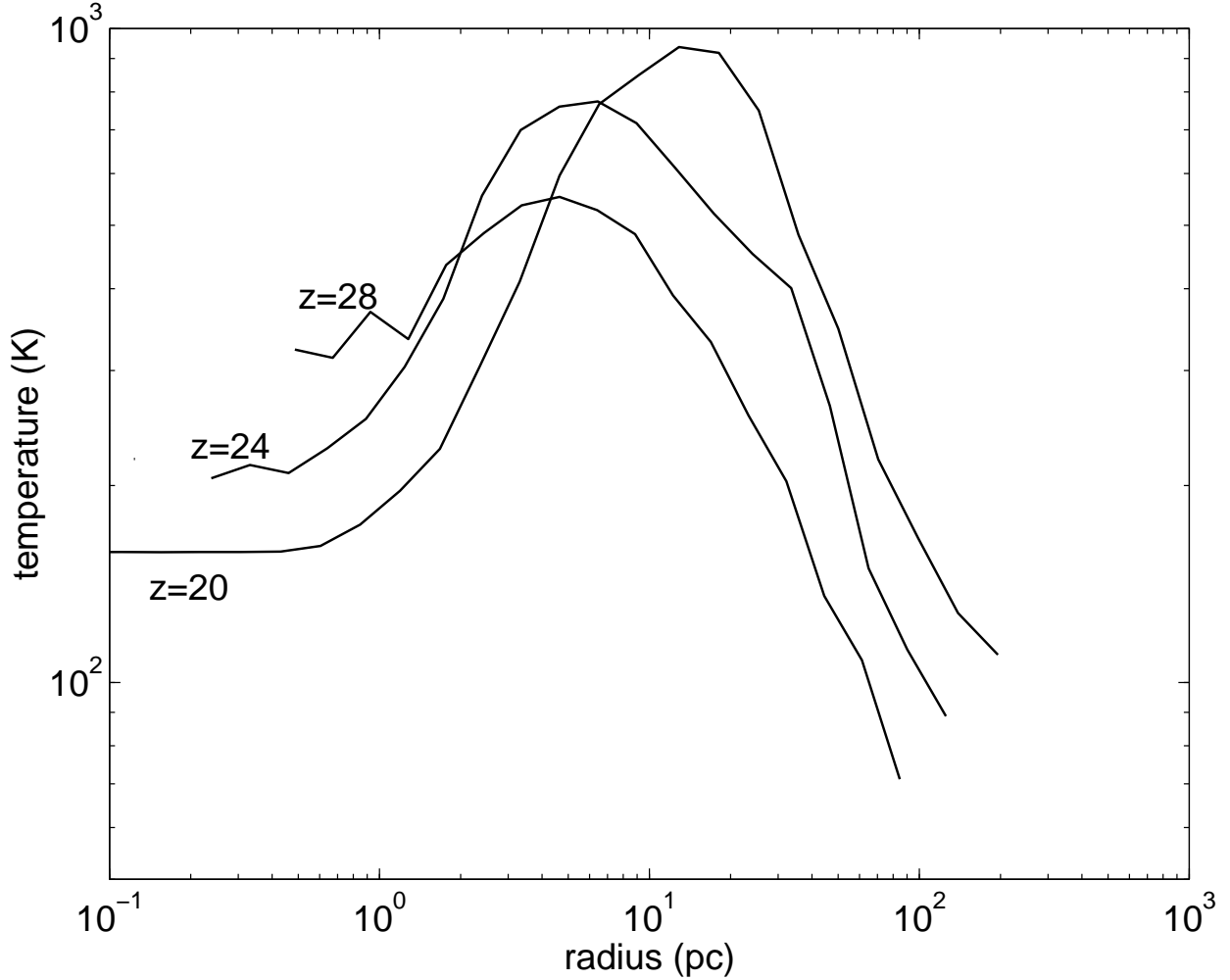


Fig. 17.— The evolution of the temperature profile of the baryons in the most massive object in a cosmological simulation at redshifts of 28, 24, and 20. These profiles correspond to the objects indicated in figure 13. The central temperature decreases as time evolves. Shock heating of gas falling into the deepening dark matter potential causes the peak temperature to increase with time, and, as the accretion shock moves outward, the peak temperature occurs at greater distances from the centre of the object.

(fig. 16). Up to this time, the gas has been relatively mildly perturbed by the growing dark matter halo. As the dark matter mass in the object increases, the deepening gravitational potential well drives up the gas density and consequently accelerates  $\text{H}_2$  production. By  $z = 24$ , the  $\text{H}_2$  abundance and temperature have increased enough that near the centre of the halo the cooling time drops below the dynamical time which is  $10^7$  years at that time. The cooling time is greater than the dynamical time very close to the centre of the object, however here the gas pressure and temperature are limited by the softening length, which is approximately 2 pc at this time. The physical state of the object is such that collapse is inevitable: the dark matter provides a deep enough potential well, and there is enough molecular hydrogen that the gas cools efficiently and free falls in the dark matter potential well. This increases the gas density and the molecular hydrogen production, thereby accelerating the  $\text{H}_2$  cooling, and a runaway feedback mechanism begins. One dynamical time later, the core temperature is just above 100 K (fig. 17), and the baryonic density exceeds the dark matter density and the object becomes self gravitating (fig. 15). At this point the conditions in the cold, dense environment are appropriate for star formation.

To test for possible numerical resolution effects, we re-sampled the initial conditions of the  $N = 2 \times 64^3$  simulation to produce an  $N = 2 \times 32^3$  distribution of particles with similar random density fluctuations. The radial profiles of various physical quantities for the most massive object were compared for both runs and found to agree well. This convergence indicates that  $2 \times 32^3$  particles provides sufficient numerical resolution, at least for the most massive object. This test suggests that a mass resolution of  $40 M_\odot$  per baryonic particle and  $650 M_\odot$  per dark matter particle is sufficient to adequately identify the first self gravitating clouds in a cosmological simulation.

Although we have discussed only one object here, we have simulated several realizations of the same cosmological model to ensure that the object presented was not anomalous in any way. Since the two different resolutions discussed above were found to be convergent, we used the lower resolution and varied only the random number seed to give different particle positions. The few most massive objects in these simulations became self gravitating at redshifts ranging from 30 to 15, and all exhibited behaviour similar to that described above: a few dynamical times after exceeding the Jeans mass,  $t_{cool}$  fell below  $t_{dyn}$  and the objects became self gravitating within approximately one dynamical time. Although the redshifts at which the objects became self gravitating covers a large range, the objects had different masses and all agreed with the  $M_{SG}(z)$  prediction of the top hat simulations to within a factor of two.

Since there exists some uncertainty in the  $\text{H}_2$  cooling rate and chemical reaction rates, we investigated the effect on the collapse of primordial objects of varying key rates. Recent determinations of the  $\text{H}_2$  cooling function have differences of a factor  $\sim 2$ , arising from uncertainty in the rotational and vibrational H- $\text{H}_2$  rate coefficients (Galli & Palla 1998). Various authors also use different rates for the formation of molecular hydrogen. We performed two simulations that differed only in the  $\text{H}_2$  cooling rate and the rate of  $\text{H}^-$  formation (which governs the total  $\text{H}_2$  abundance). Inflating  $\Lambda_{\text{H}_2}$  and the  $\text{H}^-$  formation rate each by a factor of two caused the most massive object to become self gravitating only slightly earlier ( $z = 19$  versus  $z = 17$ ) and the overall impact on the

evolution of the object was quite small.

By comparing the  $\text{H}_2$  cooling time scale to the dynamical time, Tegmark et al. (1997) argued that objects will collapse if virial temperatures are high enough to produce a critical  $\text{H}_2$  fraction of  $\sim 5 \times 10^{-4}$ . Abel et al. (1998) recovered the same abundance in self gravitating regions of objects that they simulated. However, they argued that the  $\text{H}_2$  fraction is dependent upon  $\Lambda_{\text{H}_2}$ , and that the use of different cooling functions will produce different values for the  $\text{H}_2$  abundance threshold needed for collapse. They stated therefore that their agreement in the critical  $\text{H}_2$  fraction was coincidental since they used different molecular hydrogen cooling functions. We have also found approximately the same  $\text{H}_2$  fraction present in the cores of self gravitating objects (fig. 16). The cooling function that we have used (Galli & Palla 1998) is quite similar to that used by Tegmark et al. (1997) for  $T < 400$  K, so the agreement between the  $\text{H}_2$  abundances is not surprising. The agreement between our work and that of Abel et al. (1998) does seem unexpected, since the cooling function differs markedly from the one we employed. We offer a possible explanation. A more efficient cooling function will help to maintain the number of free electrons to catalyze the  $\text{H}^-$  channel, but will also retard the production of  $\text{H}^-$  since the rate falls with temperature. These two effects conspire to minimize differences in the  $\text{H}_2$  caused by variations in the  $\text{H}_2$  cooling function. To investigate this quantitatively, we performed several different cooling functions in the semi-analytic method and recovered each author’s results. Thus, although different cooling functions will produce different temperatures, the resulting change in the  $\text{H}_2$  abundance is small.



## 6. Summary

We have studied the general framework of cooling and condensation of primordial objects in two component hierarchical cosmologies. Molecular hydrogen is the dominant coolant in primordial objects with virial temperatures between 100 K and 1000 K. Incorporating molecular hydrogen cooling into a numerical model requires explicit integration of a chemical network because of the non-equilibrium abundances of several reactants. The relevant  $\text{H}_2$  formation and cooling processes have been added to the cosmological gravitational and SPH code, Hydra. We have focused on the question of identifying haloes within which baryons can cool efficiently and in which the first stars will form, but do not attempt to model the internal structure of these first clouds in detail.

Tegmark et al. (1997) used a simple semi-analytic approach to model the density of a top hat perturbation, and integrated this along with the chemical equations and  $\text{H}_2$  cooling function to determine the evolution of the perturbation. This procedure has been followed here with a recently computed  $\text{H}_2$  cooling function as a test of the  $N$ -body code. The semi-analytic model approximates virialization by assuming that the perturbation reaches an overdensity of 200, remaining at constant physical density thereafter. We find excellent agreement between the numerical method and the semi-analytic model for cloud collapses in which the gas remains pressure supported. In cases in which efficient cooling occurs, the baryon density may substantially exceed the naive analytic value and the numerical values diverge. If, however, the baryon overdensity at virialization in the semi-analytic model is adjusted to match the  $N$ -body results, the species abundances come into good agreement once again. We find that the final, post-virialization, species abundances, densities and temperatures are insensitive to the high redshift abundance of  $\text{H}_2$ .

In accordance with the results of Tegmark et al. (1997) we find a sharp threshold (denoted by  $M_{SG}$ ) in the dark matter halo mass–redshift plane separating haloes in which gas can cool from those in which it cannot. However, our use of a current cooling function yields  $M_{SG}(z)$  values up to an order of magnitude smaller than found in the earlier work. The threshold found by the  $N$ -body method and the semi-analytic method is found to agree to within a factor of 2 over the redshift range considered.

Our primary purpose is to identify haloes in which the gas may become self gravitating. For this to occur, the baryons have to condense by a linear factor  $\sim (\Omega/\Omega_b)^{1/3}$ , leading to a disparity in the ideal softening lengths for the dark matter and gas. In order to maintain similar gravitational and hydrodynamic resolution, and to avoid spurious numerical effects, we do not allow the softening or hydrodynamic resolution to follow arbitrarily high baryon densities but instead rely on counting the number of SPH particles within an SPH smoothing length. We find this technique to be a robust indicator of whether a halo contains self gravitating gas or not. By this means we are able to adequately detect the formation of the first self gravitating gas in CDM-like cosmologies with a gas particle mass of  $\sim 40 M_\odot$ .

We have performed cosmological simulations of primordial object formation in a CDM universe. The evolution and merger histories of several objects were traced through the simulation and we

were able to show that the descriptive picture of baryon condensation in dark haloes proposed by White & Rees (1978) is an accurate representation of the relevant processes leading to the condensation of gas in dark haloes. We have shown that  $\text{H}_2$  cooling is very efficient: once the  $\text{H}_2$  abundance reaches a level such that the cooling time in the centre of a halo is less than the local dynamical time, the gas free falls in the potential well becoming self gravitating one dynamical time later. The point at which the cooling time first drops below the dynamic time agrees very well with the minimum mass threshold given by the top hat simulations. The critical  $\text{H}_2$  abundance required for collapse,  $5 \times 10^{-4}$ , is the same as found by Tegmark et al. (1997). We find that this abundance is insensitive to the details of the cooling function used.

## REFERENCES

- Abel, T., Anninos, P., Norman, M. L., & Zhang, Y. 1998, *ApJ*, 508, 518
- Abel, T., Anninos, P., Zhang, Y., & Norman, M. L. 1997, *NewA*, 2, 181
- Anninos, P. & Norman, M. L. 1996, *ApJ*, 460, 556
- Anninos, P., Zhang, Y., Abel, T., & Norman, M. L. 1997, *NewA*, 2, 209
- Blumenthal, G. R., Faber, S. M., Primack, J. R., & Rees, M. J. 1984, *Nature*, 311, 517
- Bond, J. R., Arnett, W. D., & Carr, B. J. 1984, *ApJ*, 280, 825
- Bromm, V., Coppi, P. S., & Larson, R. B. 1999, *ApJ*, 527, L5
- Carr, B. J., Bond, J. R., & Arnett, W. D. 1984, *ApJ*, 277, 445
- Couchman, H. M. P. 1986. Pregalactic activity: some consequences for galaxy formation. Ph. D. thesis, King's College, Cambridge
- Couchman, H. M. P. & Rees, M. J. 1985, *MNRAS*, 221, 53
- Couchman, H. M. P., Thomas, P. A., & Pearce, F. R. 1995, *ApJ*, 452, 797
- Dalgarno, A. & Lepp, S. 1987. Chemistry in the early universe. In M. S. Vardya & S. P. Tarafdar (Eds.), *Astrochemistry*, Reidel. Dordrecht
- Dalgarno, A. & McCray, R. A. 1972, *ARAA*, 10, 375
- Donahue, M. & Shull, J. M. 1991, *ApJ*, 383, 511
- Dove, J. E. & Mandy, M. E. 1986, *ApJL*, 311, L93
- Ferland, G. J., Peterson, B. M., Horne, K., Welsh, W. F., & Nahar, S. N. 1992, *ApJ*, 387, 95
- Forrey, R. C., Balakrishnan, N., Dalgarno, A., & Lepp, S. 1997, *ApJ*, 489, 100
- Galli, D. & Palla, F. 1998, *AA*, 335, 403
- Gnedin, N. Y. & Ostriker, J. P. 1997, *ApJ*, 486, 581
- Gould, R. J. 1964, *ApJ*, 140, 638
- Gould, R. J. & Salpeter, E. E. 1963, *ApJ*, 138, 393
- Gunn, J. E. & Gott, J. R. 1972, *ApJ*, 176, 1
- Haiman, Z., Abel, T., & Rees, M. J. 1999, [astro-ph/9903336](https://arxiv.org/abs/astro-ph/9903336)

- Haiman, Z., Rees, M. J., & Loeb, A. 1997, *ApJ*, 476, 458
- Haiman, Z., Thoul, A. A., & Loeb, A. 1996, *ApJ*, 464, 523
- Hill, J. K. & Silk, J. 1975, *ApJL*, 202, L97
- Hindmarsh, A. C. 1983. In R. S. Stepleman & M. Carver (Eds.), *Scientific Computing*, Amsterdam. North-Holland
- Hirasawa, T. 1969, *Progress of Theoretical Physics*, 42, 523
- Hollenbach, D. & McKee, C. F. 1979, *ApJS*, 41, 555
- Hutchins, J. B. 1976, *ApJ*, 205, 103
- Janev, R. K., Langer, W. D., & Evans, W. D. 1987. *Elementary Processes in Hydrogen-Helium Plasmas*. Berlin: Springer-Verlag
- Karpas, Z., Anicich, V., & Huntress 1979, *J. Chem. Phys.*, 70, 2877
- Kashlinsky, A. & Rees, M. J. 1983, *MNRAS*, 205, 955
- Knox, L. 1998, *Phys. Rev. Lett.*, 81, 2004
- Kwan, J. 1977, *ApJ*, 216, 713
- Lepp, S. & Shull, J. M. 1983, *ApJ*, 270, 578
- Lepp, S. & Shull, J. M. 1984, *ApJ*, 280, 465
- Loeb, A. 1997. The first stars and quasars in the universe. In E. P. Smith & A. Koratkar (Eds.), *ASP Conference Series - Science with the NGST*, Volume 133, pp. 73
- Martin, P. G., Schwarz, D. H., & Mandy, M. E. 1996, *ApJ*, 461, 265
- Meiksin, A., White, M., & Peacock, J. A. 1999, *MNRAS*, 304, 851
- Omukai, K. & Nishi, R. 1998, *ApJ*, 508, 141
- Osterbrock, D. E. 1974. *Astrophysics of Gaseous Nebulae*. San Francisco: Freeman and Co.
- Peebles, P. J. E. 1993. *Principles of Physical Cosmology*. Princeton: Princeton University Press
- Peebles, P. J. E. & Dicke, R. H. 1968, *ApJ*, 154, 891
- Press, W. H., Teukolsky, S. A., Vetterling, W. T., & Flannery, B. P. 1992. *Numerical Recipes in Fortran* (2 ed.). Cambridge: Cambridge University Press
- Puy, D., Alecian, G., Le Bourlot, J., Léorat, J., & Pineau des Forêts, G. 1993, *AA*, 267, 337

- Rapp, D. & Francis, W. E. 1962, *J. Chem. Phys.*, 37, 2631
- Schneider, I. F., Dulieu, O., Giusti-Suzor, A., & Roueff, E. 1994, *ApJ*, 424, 983
- Shapiro, P. R. & Kang, H. 1987, *ApJ*, 318, 32
- Shaver, P. A., Windhorst, R. A., Madau, P., & de Bruyn, A. G. 1999, *AA*, 345, 380
- Solomon, P. M. & Werner, M. W. 1971, *ApJ*, 165, 41
- Stahler, S. W. 1986, *PASP*, 98, 1081
- Stancil, P. C. 1994, *ApJ*, 430, 360
- Tegmark, M., Silk, J., Rees, M. J., Abel, T., & Palla, F. 1997, *ApJ*, 474, 1
- Thacker, R. J., Tittley, E. R., Pearce, R. R., & Couchman, H. M. P. 1998, *astro-ph/9809221*
- White, S. D. M. & Rees, M. J. 1978, *MNRAS*, 183, 341
- Wishart 1979, *MNRAS*, 187, 59P